PROTECT2024

9th International Colloquium on Performance, Protection & Strengthening of Structures Under Extreme Loading & Events

13 - 16 August 2024 | Singapore

CONFERENCE PROCEEDINGS

Organised by

NANYANG TECHNOLOGICAL UNIVERSITY SINGAPORE

NTU CEE Alumni Association

LIST OF TECHNICAL PAPERS

ID Number	Authors (s) – Paper Title
SMP-1	***Xu Wang, Jiahui Fu, Wei Wang, Guido Morgenthal*** – Performance-based Assessment Of A Novel Crashworthy Device For Protection Of Waterway Bridges From Vessel Collision
SMP-3	***Shao-Bo Kang, Yan-Ling Qin, Xiao-Fan Yu, Kun Liu*** – Influence of aluminium foam sandwich panel protective layer on the impact resistance of reinforced concrete beams
SMP-9	***Duozhi Wang, Guanglu Xu, Fengze Li, Rong Zhang*** – ”DOMINO” Progressive Fall Of Large-span Suspended Ceiling
SMP-10	***Wang Su, Anne Thymotie, Kwek Shi Ying, Yap Zhen Shyong*** – Application Of Co2 Mineralised Concrete To Reduce Embodied Carbon For A Sustainable Built Environment In Singapore
SMP-12	***Hiroshi Masuya, Michiaki Yamamoto, Yoichi Nishita, Yusuke Kurihashi*** **–** Disasters Such As Rockfalls During The Noto Peninsula Earthquake
SMP-13	***Tat-Seng Lok, Chin-Teck Ong, Alistair Crooks*** – Vehicle Security Barrier As A Counter-Measure Facility Against Deliberate And Accidental Vehicle Impact

PERFORMANCE-BASED ASSESSMENT OF A NOVEL CRASHWORTHY DEVICE FOR PROTECTION OF WATERWAY BRIDGES FROM VESSEL COLLISION

Xu Wang[1], Jiahui Fu[1], Wei Wang[1,], Guido Morgenthal[2]*

[1] School of Civil Engineering, Hefei University of Technology, Anhui Province 230009, China

[2] Chair of Modeling and Simulation of Structures, Bauhaus University Weimar, Marenstrasse 13, 99423 Weimar, Germany

Corresponding Author: Wei Wang
Email: wei.wang@hfut.edu.cn

ABSTRACT

Vessel collision has become a potential threat to the safety of waterway bridges. Many vessel-bridge collision accidents occurred in the past with serious consequences including bridge collapses and human casualties. The protection of bridges from vessel collision is therefore critical for the safety of waterway bridges. This study aims to develop a novel cost-effective crashworthy device that can absorb a large amount of impact energy during vessel collision, to assess its effectiveness for pier protection and to investigate its performance level under different vessel collision scenarios. The finite-element model of the vessel-device-pier contact system is developed and validated first. Five performance levels, i.e. elastic, low-level plasticity, mediate-level plasticity, high-level plasticity and complete collapse are defined next. The weight and impact speed of a colliding vessel are selected as two parameters and a number of samples are generated by random sampling to assess the performance level of the device under different combinations of vessel weight and speed. Finally, the weight-speed domains corresponding to five levels of performance are determined and an optimization model is proposed to determine the boundary between each two adjacent domains efficiently.

Keywords: *Vessel collision, Waterway bridge, Crashworthy device, Performance level, Weight-speed domain.*

1. INTRODUCTION

Bridge piers located in navigable waterways face increasing threats from vessel impacts due to the rising volume of vessel transportation. When a vessel collides with a pier, both the structure and the vessel sustain severe damage, potentially leading to breakout of fires[1], resulting in significant economic losses and societal impact. For instance, on February 22, 2024, at approximately 5:30 AM, an empty container vessel traveling from Nanhai, Foshan to Nansha, Guangdong province, China, struck the pier of the Lixinsha Bridge, causing the bridge deck to

collapse and resulting in five fatalities. On February 26, 2024, a container vessel struck the pier of the Francis Scott Key Bridge, resulting in the disappearance of six construction workers. In light of such incidents, the development of crashworthy devices is imperative to mitigate damage to both bridge piers and vessels involved in vessel-bridge collisions.

According AASHTO, the bridge structures shall either be protected against vessel collision forces by fenders, dikes, or dolphins as specified, or shall be designed to withstand collision force effects as specified[2]. To address this need, various types of crashworthy devices have been developed. Jiang et al [3]designed a floating steel fender system for bridge pier protection, and used an explicit dynamic finite-element analysis code to evaluate the performance of the proposed device for pier protection from vessel collisions, which showed that the device can markedly reduce the magnitude of impact force imposed on a pier column while extending the impact duration. Fan et al[4] designed a floating protection system to protect bridge piers from vessel collisions, and detailed parametric studies have shown, that the proposed device can absorb a moderate portion of energy during impact and the damage of both the ship and structures can be much alleviated. Additionally, advancements in materials science have led to the exploration of new crashworthy devices using innovative materials.

Zhu et al[5] designed a novel double functionally graded (DFG) structure using comprises of functionally graded honeycomb filler and functionally graded thickness column to protect bridge piers from vessel collisions, which showed that the device is of better and more stable crashing characteristics, can reduce the damage of both the ship and structures. Fan et al [6]designed a novel fender structure composed of steel and ultra-high performance fiber reinforced concrete (UHPFRC) for bridge pier protection, and detailed parametric studies have shown, that the device is capable of effectively decreasing impact forces and responses of a bridge as well as vessel damage. While these crashworthy devices demonstrate promising protective performance, they often come with high costs or remain in the theoretical design phase, posing challenges for practical implementation.

The authors have previously proposed steel frame crashworthy structures consisting of steel beams with I cross-sections [7–9]. These structures have been verified to offer excellent protective efficacy and withstand tremendous impact forces at a relatively low cost, making them highly promising for practical applications. To facilitate the design of novel crashworthy devices, this study evaluates their performance by analyzing plastic deformation resulting from head-on vessel impacts with varying weights and speeds, utilizing a simplified vessel-device-pier impact model. Subsequently, weight-speed domains are derived, and an optimization model for determining these domains is developed.

2. NUMERICAL MODEL

In this paper, a barge developed by the authors in the early studies [10] is employed as the colliding vessel. The computationally efficient simplified barge-device impact model for analyzing the dynamic behavior of a novel crashworthy device under barge collision is then introduced.

2.1. The colliding barge vessel

The vessel employed here is a typical Jumbo Hopper barge which is adopted in the AASHTO Guide Specification [11], where the general configuration and geometric dimensions of

different structural components are described in detail. The empty and fully-loaded weight of the barge are 181.4 tons and 1723.7 tons.

The authors developed the finite-element model of the barge vessel in the early studies, as illustrated in Figure 1 where the outskin of the barge is modelled by shell elements with thickness of 0.012 m, whilst the inner trusses inside the bow are modelled using beam elements. The inner trusses are welded to the outskin.

As only head-on collision scenarios are considered here, the barge bow generally experience significant plastic deformation whilst the rear part of the barge is not expected to have marked deformation. For this reason, the structural components of the barge bow are modelled using plastic material model whilst the rear part is modelled using rigid material. The strain-stress curve of the barge steel is plotted in Figure 2 as per Ref. [12]. The deformation process of the barge during the actual collision can be more accurately modelled by using the stress-strain curve shown in Fig. 2. The mass density, Young's modulus, Poisson's ratio, yield stress and failure strain of steel are taken to be 7910.0 kg/m^3, 207.0 GPa, 0.33, 248.0 MPa and 0.25, respectively.

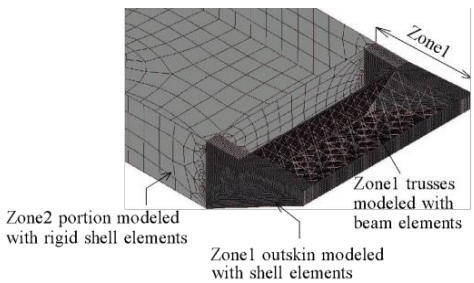

Figure 1. Finite-element model of the barge vessel [10].

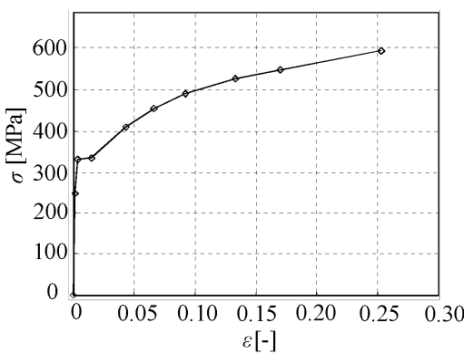

Figure 2. Stress-strain curve of the barge steel [10].

2.2. The crashworthy device

The weight of barges is typically substantial, resulting in high-impact energy during collisions. To minimize damage to both the barge and the pier, a crashworthy device should be capable of dissipating a significant portion of the impact energy through plastic deformation. Drawing inspiration from this concept, the crashworthy device depicted in Figure 3 has been designed.

The device consists of an impact cap connected to piers via a series of steel beam frames with an I-cross-section. The cap is positioned to float on the water's surface, supported vertically by slender piles or floating elements. Each steel beam leg is joined through bending stiff connections, such as welds, ensuring that a force applied to the cap generates bending moments within the steel structure. Multiple layers of beam units can be installed to enhance energy dissipation capacity and achieve the desired elastic and plastic deformation behavior. In Figure 3, three planes are depicted, which can be mutually braced to prevent out-of-plane stability failure.

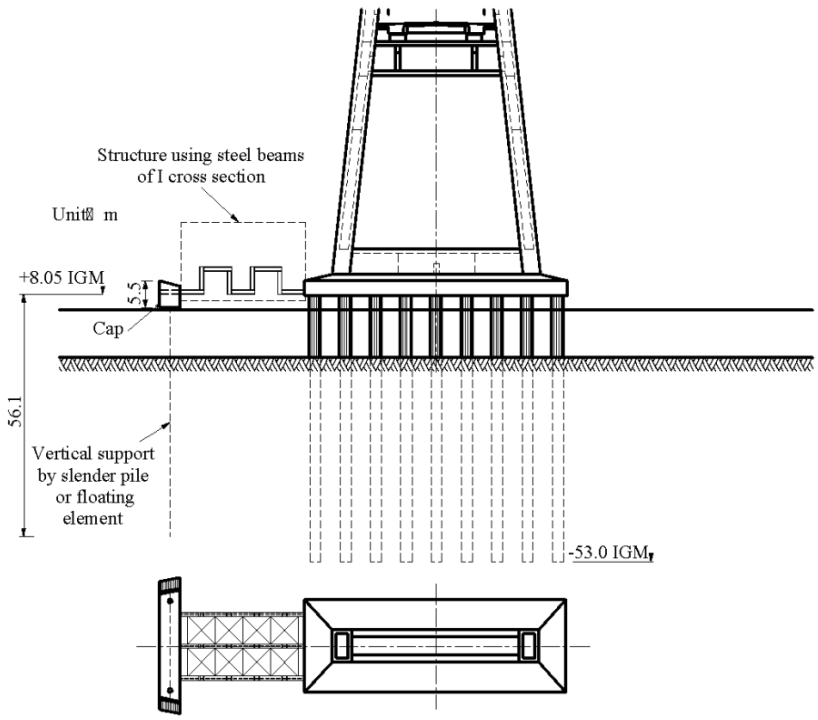

Figure 3. The structure connecting the cap and the bridge pier using steel beams of I-cross-section [7].

The device is modeled using beam elements with a uniform meshing size of 0.1 m. The steel is simulated using the piecewise linear plasticity material model and a bi-linear stress–strain curve is used. Four material parameters, i.e. yield stress (σ_y), ultimate stress (σ_u), elastic modulus (E_S) and hardening modulus (E_t), shall be defined. In this study, the S355 steel is used. The values of related material parameters are tabulated in Table 1.

The corresponding 3-D FE model of the device is demonstrated in Figure 4, where the element types of different components are demonstrated as well. In this paper, the width of I-cross-section is taken to be 1.1m, and other geometric parameters, including heights and thicknesses of the flanges and webs, and the length of each steel beam of the device, are taken based on normative proportions, as shown in Table 2.

Table 1 Material parameters of S355 steel

Variable	Value	Source
ρ = mass density	7850 kg/m^3	Eurocode 3[13]
E_S = elastic modulus	210 GPa	Eurocode 3[14]
E_t = harden modulus	2.1 GPa	Eurocode 3[15]
σ_y = yielding stress	335 MPa	Eurocode 3[14]
σ_u = ultimate stress	470 Mpa	Eurocode 3[14]
ε_y = yielding strain	0.0016	Calculated
ε_u = ultimate strain	0.066	Calculated

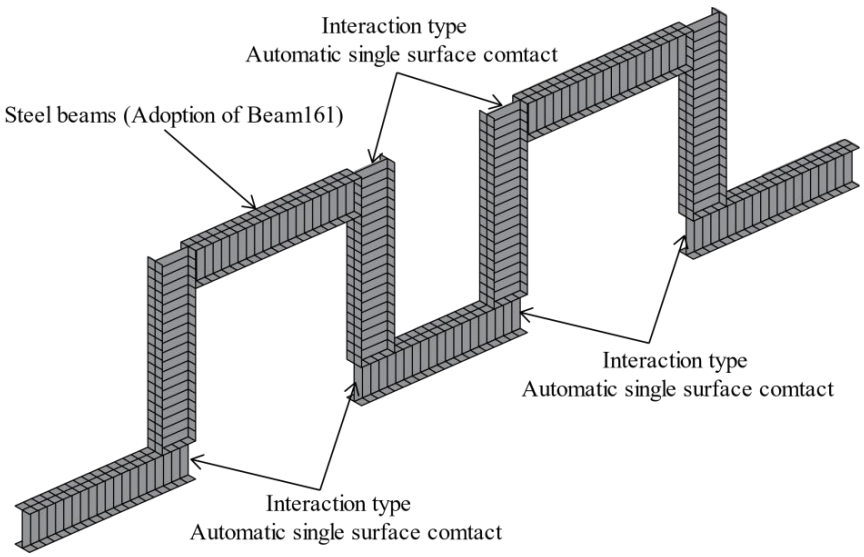

Figure 4. The FE model of the proposed device.

Table 2. Geometrical parameters of I-beam sections.

Variable	Value
width of I-sections	1.1 m
height of I-section	0.733 m
thickness of section flanges	0.0733 m
thickness of section web	0.1467 m
length of each steel beam	8.0 m

For simplification purposes, several assumptions are adopted herein: (1) the lateral resistance of the cap's supporting structure is ignored, (2) the pylon foundation is assumed to be rigid, and (3) the cap is assumed to be rigid and is modeled using a lumped mass. Based on these assumptions, the structure shown in Figure 1 can be simplified into the cap-steel-beam

structure, as shown in Figure 5. The cap can move freely in the horizontal direction whilst its vertical movement is constrained.

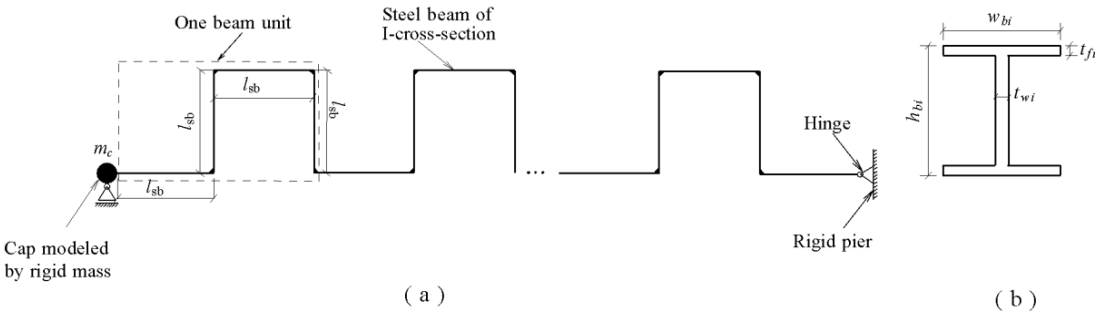

Figure 5. Configuration of (a) the cap-steel-beam structure and (b) I-cross-section of steel beams. N_{bu}: number of beam units in one plane; l_{sb}: length of each single steel beam; m_c: cap mass [7].

2.3. The simplified vessel-device-pier impact model

The authors previously introduced a nonlinear mass-spring model (MSM) as a simplified representation of the nonlinear and complex finite element (FE) barge model. The pier column is discretized into a series of masses and fiber beams. By coupling these two simplified models, it becomes possible to efficiently and accurately compute nonlinear barge-pier impact processes. This coupled model is termed the coupled multi-degree-of-freedom model (CMM). Further details can be found in Ref. [10]. The simplified vessel-device-pier impact model is developed based on CMM for dynamic analysis of the proposed crashworthy device subjected to barge impact. The steel beams are modeled using discrete masses and fiber beam elements, while the MSM is coupled with the simplified crashworthy device at the cap. The effects of material non-linearity are considered using a bi-linear stress-strain curve to describe the material property of steel, whilst geometric non-linearity caused by large displacements is considered by corotational approach. The simplified vessel-device-pier impact model is illustrated in Figure 6.

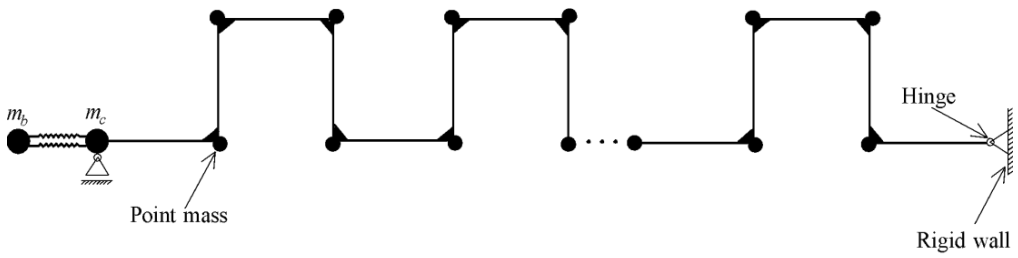

Figure 6. Simplified impact model based on CMM for dynamic analysis of the proposed device subjected to barge impact [7].

3. NUMERICAL RESULTS

Several different performance levels of the proposed device under barge impact is defined based on its degree of plasticity, and the weight-velocity domain of the barge corresponding to each performance level is determined. An optimization model is proposed to determine the boundary curve between each two adjacent domains efficiently.

3.1. Definition of performance levels

Depending on the material properties of steel and the geometrical parameters of the I-cross-section, it is possible to define two bending moments, the yielding moment (M_y) and the ultimate bending moment (M_u). The My corresponds to the state when the cross-section strain reaches the yield strain of steel, and the Mu corresponds to the state when the cross-section strain reaches the ultimate strain (maximum allowable strain) of steel. In this paper, the maximum bending moment of the steel frame section during barge collision is defined as M. Based on the maximum bending moment, the performance of the device is divided into five levels, i.e. elastic ($M < M_y$), low-level plasticity ($M_y \leq M < M_y + r_1 \times (M_u - M_y)$), moderate-level plasticity ($M_y + r_1 \times (M_u - M_y) \leq M < M_y + r_2 \times (M_u - M_y)$), high-level plasticity ($M_y + r_2 \times (M_u - M_y) \leq M < M_y + 1.0 \times (M_u - M_y) = M_u$), and complete collapse ($M > M_u$). The values of r_1, and r_2 which are smaller than 1.0 can be arbitrarily defined. In this paper, we take r_1 as 0.3 and r_2 as 0.7.

3.2. The weight-speed domains

In this paper, the vessel speed (v_0) and the vessel weight (m_v) are selected as the two design parameters, and a two-dimensional v_0- m_v domain is defined. The vessel weight varies between 181.4 tons and 1723.7 tons whilst the speed varies between 1.03 m/s (minimum vessel speed) to 3.09 m/s (maximum vessel speed). A random sampling method was used to generate 900 impact scenarios with different combinations of v_0 and m_v, and the maximum bending moment (M) within the device during barge collision corresponding to each scenario is calculated using the simplified dynamic model described in Figure 5, which is then used to evaluate the performance level of the device based on the definition in Section 3.1.

The v_0- m_v domain corresponding to each performance level is demonstrated in Figure 7, where four sub-domains, namely the elastic domain (black), the low-plasticity domain (blue), the medium-plasticity domain (red), and the high-plasticity domain (green) are identified based on the generated samples. Three boundary curves can be clearly figured out. Due to the relatively large cross-section dimension of the steel beam which results in high structural stiffness, the maximum bending moment (M) of the crashworthy device still does not reach the ultimate bending moment (M_u), even at the maximum vessel weight and the highest vessel speed. Therefore, the sub-domain corresponding to the complete collapse of device does not appear in the v_0- m_v domain.

The determination of the extent of damage on the device during impact requires a nonlinear dynamic analysis with a couple of minutes, which leads to a substantial computational cost when a large amount of samples is needed to determine the boundary curves in the v_0- m_v

domain. Therefore, an optimization model is developed to determine the boundary curves in the v_0- m_v domain efficiently yet accurately.

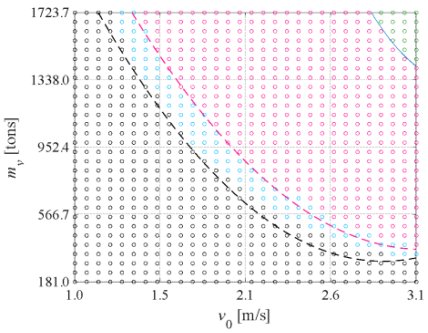

Figure 7. The weight-speed domains corresponding to different performance levels of the crashworthy device under barge collision.

3.3. Optimization model for sub-domain determination

From Figure 6, it can be seen that each boundary curve is very similar to a quadratic parabola, so this paper assumes that the functional expression of the boundary curve is $m_v = a \times v_0^2 + b \times v_0 + c$, where a, b and c are three unknown coefficients to be determined.

Five points, corresponding to different v_0- m_v combinations, are selected on the defined parabolic curve, the coordinates of which are defined to be: (m_1, v_1), (m_2, v_2), (m_3, v_3), (m_4, v_4), and (m_5, v_5). The maximum bending moment (M) corresponding to each point is defined as M_1, M_2, M_3, M_4, and M_5, respectively. The objective of the proposed optimization model is to minimize the error (r) between M_i (i=1,2,…5) and M_b which represents the boundary value of the maximum bending moment corresponding to each performance level based on the definition in Section 3.1:

$$r = \sum_{i=1}^{5} \left(M_i - M_b \right)^2 \tag{1}$$

The parameters for optimization are the three unknown coefficients, i.e. a, b and c. The goal is to determine the optimum set of a, b and c so that the value of r is minimized.

In this paper, the Particle Swarm Optimization (PSO) algorithm is used to solve the proposed optimization model. The PSO requires the determination of three user-defined parameters, i.e. weights (ω), personal learning coefficient (cp) and global learning coefficient (cg), which are taken as 1.0, 1.0 and 2.0 in this study, respectively. The values of a, b, and c corresponding to different performance levels are subsequently obtained through an iterative process aiming at minimizing the value of r. The iterative process of the PSO algorithm is shown in Figure 8, from which it can be seen that basically fast convergence and stability can be achieved in 70 iterations.

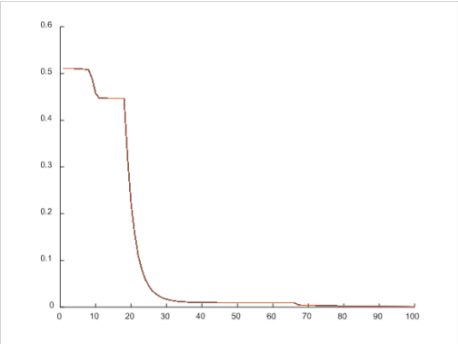

Figure 8. PSO iterative process for minimizing the optimization objective.

Based on the proposed optimization strategy, the optimum values of a, b and c corresponding to the first boundary curve are 483.0, 2790.6 and 4329.9, respectively, and the corresponding parabolic curve in the v_0- m_v domain is plotted in Figure 6 with black line. The same process is executed to determine the other two boundary curves, which are plotted with red line and green line in Figure 6, respectively. The functions of three parabolic curves are listed as follows:

$$m_v = 483.0 \times v_0^2 - 2790.6 \times v_0 + 4329.9 \tag{2}$$

$$m_v = 440.5 \times v_0^2 - 2756.7 \times v_0 + 4680.5 \tag{3}$$

$$m_v = 1492.0 \times v_0^2 - 9950.6 \times v_0 + 17917.7 \tag{4}$$

The result shows that the optimum parabolic curves match very well with the actual boundary curves, which demonstrates the effectiveness of the proposed optimization model in determining the boundary curves in the v_0- m_v domain without the efforts for running a large amount of simulations.

CONCLUSIONS

This paper defines five different performance levels based on the degree of plastic deformation of the device, i.e. elastic, low-level plasticity, moderate-level plasticity, high-level plasticity, and complete collapse. Using the weight and impact speed of a colliding vessel as design parameters, a series of experimental conditions were generated through random sampling. These experimental conditions were evaluated using the coupled multi-degree-of-freedom mode (CMM) established in previous studies to determine the performance level corresponding to each condition. The weight-speed domains corresponding to the five performance levels was identified, and an optimization model was proposed to effectively determine the boundaries between each adjacent domain.

The study indicates that there are boundary curves resembling parabolic shapes between different weight-speed domains. Therefore, this paper establishes a mathematical optimization model with three unknown coefficiencies of a parabolic function as the optimization parameters, aiming to rapidly and accurately determine the boundary curve of the weight-speed

domains. The results indicate that the optimal parabolic curve generated using the optimization model closely matches the actual boundary curve. The effectiveness of the proposed optimization model in determining the boundary curve within the weight-speed domains has been demonstrated.

However, the I-beam cross-section size selected in this paper is too large, resulting in the destruction stage not being reached even at the maximum kinetic energy, for this reason, the subsequent discussion should be carried out with the I-beam cross-section size as a design parameter, and the optimization model should be established under different I-beam sizes.

ACKNOWLEDGMENTS

The author wishes to thank the National Natural Science Foundation of China under contract number 52008144 and the Fundamental Research Funds for Central Universities of HFUT under contract numbers of JZ2022HGTB0290, JZ2022HGTB0277 and JZ2022HGTB0355 which provide the research funding for the authors to conduct this study.

REFERENCES

[1] V.K.R. Kodur, A.M. Gil, M.Z. Naser. Fire-induced collapse of an I-95 overpass in Philadelphia: Causes, collapse mechanism, and mitigation strategies[J]. Engineering Structures, 2024, 303.

[2] AASHTO. LRFD Bridge Design Specifications. Washington, DC, USA; 2009.

[3] Jiang H, Chorzepa M G. (2016) Case study: Evaluation of a floating steel fender system for bridge pier protection against vessel collision. Journal of Bridge Engineering 21(11): 05016008.

[4] Fan W, Yuan W, Li G. (2011) Numerical analysis of floating protection system for bridge structure subjected to vessel impact. International Conference on Electric Technology and Civil Engineering (ICETCE). IEEE: 476-479

[5] Zhu G, Li S, Sun G. (2016) On design of graded honeycomb filler and tubal wall thickness for multiple load cases. Thin-Walled Structures 109: 377-389.

[6] Fan W, Guo W, Sun Y. (2018) Experimental and numerical investigations of a novel steel-UHPFRC composite fender for bridge protection in vessel collisions. Ocean engineering 165: 1-21.

[7] Wang W, Morgenthal G. (2018) Novel Crashworthy Device for Pier Protection from Barge Impact. Advances in Civil Engineering 2018: 1-15.

[8] Wang W, Morgenthal G, Kraus M. (2020) Numerical evaluation of a novel crashworthy device for pier protection from barge impact. Engineering Structures 212: 110535.

[9] Wang W, Zhou F, Zhou R X. (2022) Numerical evaluation of novel crashworthy devices for protection of RC piers subjected to vessel impact. Ocean Engineering 259: 111857.

[10] Wang W, Morgenthal G. (2018) Development and assessment of efficient models for barge impact processes based on nonlinear dynamic finite element analyses. Engineering Structures 175: 617-627.

[11] American Association of State Highway and Transportation Officials (AASHTO 2009) Guide specification and commentary for vessel collision design of highway bridges. Washington, DC, USA.

[12] Consolazio GR, Cowan DR. (2003). Nonlinear analysis of barge crush behavior and its relationvessel to impact resistant bridge design. Computers and Structures 81: 547–557.

[13] Eurocode 3 - Design of steel structures - part 5: Piling. 2006.

[14] Eurocode 3 - Design of steel structures - part 1-2: General rules - structural fire design. 2005.

[15] Eurocode 3 - Design of steel structures - part 1-5: Plated structural elements. 2006.

Influence of aluminum foam sandwich panel protective layer on the impact resistance of reinforced concrete beams

Shao-Bo Kang [1], Yan-Ling Qin [2], Xiao-Fan Yu [3], Kun Liu [*]

[1] Prof., School of Civil Engineering, Chongqing University, Chongqing 400045, China, kang0119@cqu.edu.cn

2 Ms., School of Civil Engineering, Chongqing University, Chongqing 400045, China, qinyanling@cqu.edu.cn

3 Ms., School of Civil Engineering, Chongqing University, Chongqing 400045, China, yuxiaofan@cqu.edu.cn

[*] Mr., School of Civil Engineering, Chongqing University, Chongqing 400045, China, liuk@cqu.edu.cn

ABSTRACT

This study investigates the impact resistance enhancement of reinforced concrete beams through the application of an aluminium foam sandwich panel protective layer. Impact tests were conducted on three specimens: an unprotected reinforced concrete beam, one with an aluminium foam protective layer, and another with a sandwich panel protective layer, to analyse their dynamic responses and failure modes. Test results revealed that both the aluminium foam and sandwich panel effectively shielded the reinforced concrete beams from severe damage under impact, leading to a transition in failure pattern from shear to flexure-shear. The beams with the protective layer exhibited lower peak forces and reduced mid-span deformation compared to the unprotected beam. Moreover, the protective effects of the aluminium foam and sandwich panel were found to be nearly equal. This research serves as a valuable reference for designing reinforced concrete beams with a sandwich panel protective layer to enhance resistance against impact loads.

Keywords: *Reinforced Concrete Beams, Aluminium Foam Sandwich Panel, Drop Hammer Impact Test, Impact Response, Energy Absorption Capacity.*

[*] School of Civil Engineering, Chongqing University, Chongqing 400045, China (corresponding author).

E-mail: liuk@cqu.edu.cn

1. INTRODUCTION

Reinforced concrete structures may be subjected to various types of impact loads, including those from natural disasters and ballistic missiles [1, 2]. Therefore, it is significant to study the dynamic behaviour and failure mechanism of reinforced concrete members under low-velocity impact. Current investigations have extensively studied the dynamic response of reinforced concrete beams against impact. Fujikake et al. [3] experimentally studied the influence of impact energy and reinforcement ratio on the dynamic response of reinforced concrete beams, demonstrating that an increase in the impact energy increased both peak force and deformation. Pham et al. [4, 5] investigated the influence of global stiffness and contact stiffness on beam responses through experimental tests and numerical simulations. Experimental results showed that the deflection of beams decreased with the increasing overall stiffness, and the peak force increased with the increasing contact stiffness. Zhan et al. [6] conducted experimental tests to study the effect of drop hammer height on the dynamic response of beams, revealing a positive correlation between the deflection of beams and impact energy.

Reinforced concrete members are susceptible to shear failure when exposed to impact loads, posing a challenge in ensuring the safety of reinforced concrete structures under such conditions. As a result, several approaches have been suggested to enhance the impact resistance of reinforced concrete members, including applying composite materials to the surface [7, 8] or substituting normal concrete with high-strength concrete [9, 10]. Nevertheless, there is currently limited research on improving the impact resistance of reinforced concrete members by employing a protective layer on the impact surface. Aluminium foam, known for its low density and high energy absorption capability due to its porous structure [11-13], can reduce the impact force and absorb energy by undergoing obvious plastic deformations, thereby minimizing the damage to reinforced concrete members. Schenker et al. [14, 15] studied the dynamic response of reinforced concrete beams and slabs with an aluminium foam protective layer under impact. The test results indicated that the aluminium foam played a crucial role in reducing impact forces and effectively safeguarding reinforced concrete members. Notably, the aluminium foam, commonly utilized in sandwich panels as a core material, exhibited excellent impact resistance [16-18]. However, present investigations mainly focus on the blast resistance of reinforced concrete members with a protective layer, there is still a lack of research on the impact resistance of reinforced concrete beams incorporating a sandwich panel protective layer.

This study used a sandwich panel comprising a stainless steel upper sheet, an aluminium foam core, and a carbon steel lower sheet to protect reinforced concrete beams. A series of drop hammer impact tests was conducted on a normal reinforced concrete beam and two beams with a protective layer to assess their impact resistances, emphasizing the dynamic response and failure pattern of the beams. The research contributes significantly to enhancing the impact resistance of reinforced concrete beams with a protective layer.

2. EXPERIMENTAL PROGRAM

2.1. Beam design and test preparation

Three beams were designed for drop hammer impact tests, comprising a reinforced concrete beam, a reinforced concrete beam with an aluminium foam protective layer, and a reinforced concrete beam with a sandwich panel protective layer. The dimensions and reinforcement details of the beams are presented in Figure 1. The sandwich panel consisted of a stainless steel sheet as the upper sheet, a carbon steel sheet as the lower sheet and an aluminium foam as the core, bonded together with epoxy resin adhesive. The width, height and length of the beams were 100 mm, 200 mm and 1900 mm, respectively. The thicknesses of the upper sheet, lower sheet and aluminium foam core were 1.5 mm, 3 mm and 20 mm, respectively. The aluminium foam had a density of 0.4-0.5g/cm³. The diameters of the top and bottom longitudinal reinforcement were 12 mm and 16 mm, respectively, while the stirrups were 6 mm in diameter with a spacing of 75 mm.

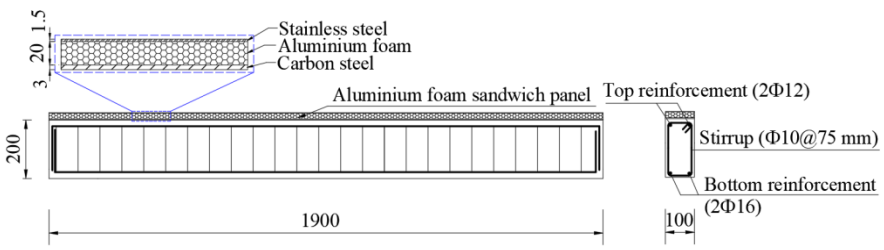

Figure 1. Details of the specimen with a sandwich panel protective layer.

Table 1 shows the details of the beams used in the impact tests, featuring three types of protective layers: no protection, aluminium foam, and sandwich panel. Each beam designation consists of three parts: the beam identifier, the impact energy, and the type of protective layer. For example, B-5500-SP signifies a beam protected by a sandwich panel under a 5500 J impact energy.

Table 1. Parameters of specimens for impact tests

Specimens	Cross-section of beams (mm)	Type of protective layer	Weight of drop hammer (kg)	Impact energy (J)
B-5500	1900×100×200	None	206.75	5500
B-5500-AF		Aluminium foam		5500
B-5500-SP		Sandwich panel		5500

2.2. Test setup

Impact tests were conducted using a DHR940 Drop Hammer, illustrated in Figure 2. A cylindrical flat drop hammer with an 80 mm diameter and a 206.75 kg counterweight was employed. A load cell was integrated into the drop hammer for precise measurements. To

mitigate localized damage, a rigid steel plate with dimensions of 100 mm in length, 100 mm in width, and 20 mm in height was positioned at the top of beams. The beams, with a clear span of 1600 mm, were simply supported, and steel cables were installed at the supports to prevent upward rebounding after the impact. A high-speed camera was used to capture the failure process of the beams. Speckle markings were pasted in a 400 mm × 200 mm area on the front surface of the beams. The mid-span displacement-time history of the beams was obtained by Digital Image Correlation (DIC) equipment.

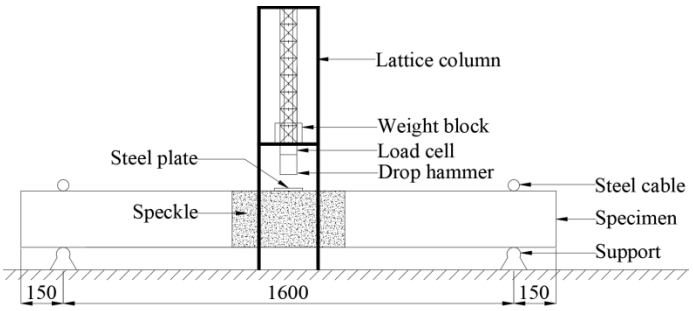

Figure 2. Test setup for beams under impact.

2.3. Material characteristics

The compressive properties of aluminium foam were obtained through compression tests following GB/T 7314-2017 [19]. The aluminium foam samples, with dimensions of 20 mm in height and diameter, a density of 0.47 g/cm^3 and a 4 mm average cell size, underwent testing at a 1.2 mm/min rate. The stress-strain curve of the aluminium foam exhibited three stages, as shown in Figure 3, i.e., the elastic stage (stage I), plateau stage (stage II) and densification stage (stage III). The long plateau stage indicated the excellent energy absorption of the aluminium foam. In this study, the yield stress, plateau stress and densification strain of the aluminium foam were quantified to be 9.3 MPa, 7.3 MPa and 0.6, respectively.

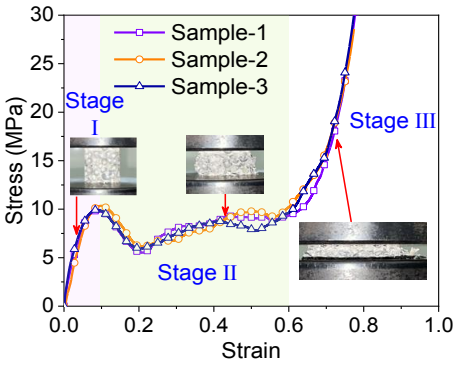

Figure 3. Stress-strain curves of aluminium foam samples.

The mechanical characteristics of steel sheets and rebars were determined by using uniaxial tensile tests according to GB/T 228-2010 [20], with a consistent loading rate of 5 mm/min. Table 2 provides a summary of the mechanical properties of the steel sheets and rebars. The compressive strength of concrete was determined through the compressive test on cubic samples of 100 mm in dimensions. The average compressive strength of concrete was determined to be 56.1 MPa.

Table 2. Mechanical properties of steel plates and reinforcement

Steel grade	Material	Thickness or diameter (mm)	Young's modulus (GPa)	Poisson's ratio	Yield stress (MPa)	Ultimate stress (MPa)
Stainless steel	Upper sheet	1.5	130	0.3	256	768
Carbon steel	Lower sheet	3	460	0.3	297	454
Q355 carbon steel	Stirrups	6	200	0.3	348	486
	Longitudinal reinforcement	12	197	0.3	458	658
		16	201	0.3	432	594

3. EXIPERIMENTAL RESULTS AND DISCUSSIONS

3.1. Force-time history

It is evident from Figure 4 that the type of protective layers significantly influenced the force-time history of the beams. For B-5500, the impact force increased rapidly initially. Following the first peak force of 615.4 kN, a slight rebound of the drop hammer caused the impact force to drop to nearly zero. Subsequently, the impact force increased to a second peak force before it decreased to zero once again. Thereafter, the drop hammer and the beam moved together, and the force-time curve entered the plateau stage. Afterwards, the impact energy was primarily converted into the internal energy of the beam, resulting in the drop hammer rebounding and a gradual reduction of the force. Finally, the force decreased to zero at around 0.035 s, indicating the separation of the drop hammer from the beam. Notably, there was a force increase between 0.02 s and 0.26 s due to the contact between the bottom of the beam and the rubber block on the support.

Compared to B-5500, the initial increase in the impact force of B-5500-AF was relatively gradual, with the first peak force of B-5500-AF noticeably lower than that of B-5500. This difference could be attributed to the porosity of the aluminium foam on the top face, which significantly reduced the contact stiffness between the drop hammer and the beam. Moreover, the pore structure of the aluminium foam led to force fluctuations during the initial phase. Subsequently, as the aluminium foam was densified, the primary energy absorbing component was shifted from the aluminium foam to the reinforced concrete beam, causing a rapid drop in the force. Afterwards, the drop hammer and the beam moved together, and the curve entered the plateau stage with slight oscillations. Finally, the force gradually decreased to zero.

The initial increase in the impact force of B-5500-SP was faster than that of B-5500-AF, attributed to the higher contact stiffness resulting from the stainless steel sheet between the

drop hammer and the beam. The peak forces of B-5500-SP and B-5500-AF were in close proximity. This similarity resulted from the fact that, during the initial stage, the primary energy absorbing component in both B-5500-SP and B-5500-AF was the aluminium foam. Following the attainment of the first peak force, the force-time curve of B-5500-SP was similar to that of B-5500-AF. Notably, the plateau stage of both B-5500-SP and B-5500-AF was slightly higher than that of B-5500, as more severe damage was sustained by B-5500 before the curve reached the plateau stage.

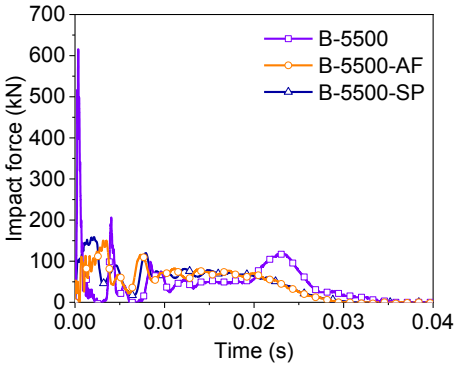

Figure 4. Impact force-time history of beams with different protective layers.

3.2. Failure process and final failure patterns

During testing, the failure process of beams near the mid-span was captured by a high-speed camera operating at a shooting frequency of 5000 frames per second. The initiation of contact between the drop hammer and the steel plate was taken as 0 ms.

The failure process of B-5500 is illustrated in Figure 5(a). Initially, two diagonal cracks appeared at the bottom of B-5500. Subsequently, multiple flexural cracks developed at the bottom of B-5500 at 5 ms, accompanied by a significant widening of the diagonal cracks. Additionally, the concrete in the impact zone was immediately crushed. The width of both flexural and diagonal cracks continued to increase, with the spalling of concrete observed near the bottom of B-5500. At 20 ms, the two diagonal cracks were further widened and became the major crack. B-5500 then began rebounding at 24 ms, leading to the separation of the drop hammer and B-5500 at 35 ms. Notably, diagonal cracks preceded flexural cracks during the impact process, and their width consistently exceeded that of flexural cracks, indicating that the diagonal cracks were the primary crack.

B-5500-AF exhibited no significant cracks at 0.6 ms, as shown in Figure 5(b). At 5 ms, B-5500-AF showed vertical microcracks that were smaller in width in comparison to B-5500, with uncrushed concrete in the contact zone and evident aluminium foam compression. Subsequently, the flexural cracks were progressively widened and propagated, with slight crushing of concrete in the contact area. Flexural and diagonal cracks developed in the subsequent impact, and crushing and spalling of concrete was observed as well. Notably, after 5 ms, the compressive deformation of the aluminium foam remained consistent. Finally, the impactor rebounded and then was separated from the beam.

Figure 5(c) presents the failure process of B-5500-SP. At 2 ms, noticeable bending deformations occurred in the upper sheet, along with compressive deformations in the aluminium foam. Then, the failure process of B-5500-SP was similar to that of B-5500-AF. Notably, in the initial stage, the lower sheet of the sandwich panel was debonded from the reinforced concrete beam due to its high stiffness. Compared to B-5500, the emergence of cracks in B-5500-AF and B-5500-SP was postponed. Furthermore, while the primary cracks in B-5500 consisted of two diagonal cracks, beams with protective layers exhibited flexural cracks in the primary crack. Hence, the incorporation of aluminium foam or a sandwich panel as a protective layer shifted the failure mode from brittle shear failure to ductile flexural failure.

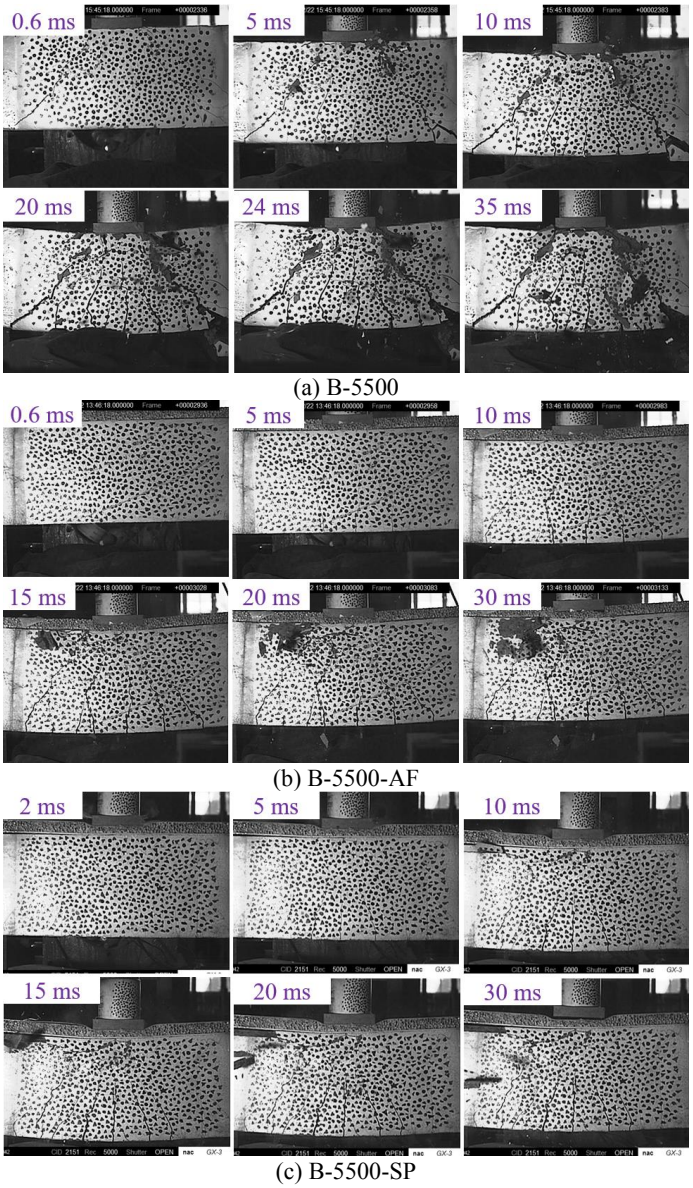

Figure 5. Failure process of specimens.

Figure 6 shows the final failure mode of the beams. As shown in Figure 6(a), B-5500 experienced shear failure upon impact, with the concrete in the contact region being crushed and spalled off. Furthermore, obvious vertical and diagonal cracks appeared at the mid-span, with two diagonal cracks propagating through the entire cross-section of the beam and a shear plug forming around the impact zone. As shown in Figures 6(b) and (c), compared with B-5500, B-5500-AF and B-5500-SP did not exhibit diagonal cracks and crushing of concrete in the impact contact area was obviously less. Therefore, the protective layer notably mitigated the damage to the reinforced concrete beams and shifted the failure mode from shear failure to flexural-shear failure. Notably, the damage at the mid-span remained consistent between B-5500-AF and B-5500-SP, highlighting a similar protective effect of the aluminium foam and sandwich panel on the reinforced concrete beams.

(a) B-5500

(b) B-5500-AF

(c) B-5500-SP

Figure 6. Failure pattern of specimens.

3.3. Mid-span displacement-time history

Figure 7 shows the mid-span displacement-time history of the beam. The displacement-time histories of all beams followed a similar pattern, with displacement rapidly rising to its peak and subsequently decreasing to residual levels. Notably, the slight vibration of the beam at the support led to oscillations in the curve due to the relatively loose cables on both sides. The mid-span displacement curve of B-5500 exhibited the greatest magnitude among the three beams, while the mid-span displacement curves of B-5500-AF and B-5500-SP were close to each other. Thus, the inclusion of aluminium foam and the sandwich panel led to a notable reduction in mid-span displacement, signifying the effective protective role of these layers for the reinforced concrete beam.

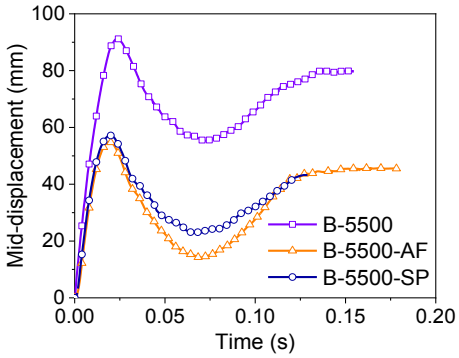

Figure 7. Mid-span displacement-time histories of beams with different protective layers.

3.4. Effect of protective layer

Figure 8 presents the peak and plateau forces of beams with different protective layers. The peak force of B-5500 was 615.4 kN, 4.1 and 3.8 times as much as those of B-5500-AF and B-5500-SP , respectively. It was due to the fact that the stiffness of the aluminium foam and sandwich panel was low, reducing the contact stiffness between the drop hammer and the beam. The peak forces for B-5500-AF and B-5500-SP were close, 149.7 kN and 160.8 kN, respectively. However, the plateau force of B-5500-AF and B-5500-SP was higher than that of B-5500, increased by 38.2% and 36.8%, respectively. The reason was that there was less initial damage on B-5500-AF and B-5500-SP compared to B-5500. Therefore, both the aluminium foam and sandwich panel effectively lowered the peak forces and increased the plateau forces, acting as a buffer during impact.

Figure 8(b) presents the influence of the protective layer type on the mid-span deformation of beams. When the reinforced concrete beam was designed with an aluminium foam protective layer, the maximum mid-span displacement decreased by 39.9% from 91.3 mm to 54.9 mm, and the residual mid-span displacement decreased by 45.2% from 79.8 mm to 43.7 mm. Similarly, with a sandwich panel protection, both maximum and residual displacements decreased by 37.3% and 47.0% to 57.2 mm and 42.3 mm, respectively. Therefore, both the aluminium foam and sandwich panel effectively mitigated the mid-span deformation of reinforced concrete beams. Notably, the maximum and residual displacements of B-5500-AF and B-5500-SP were close to each other, suggesting comparable protective efficacy of aluminium foam and sandwich panels on reinforced concrete beams.

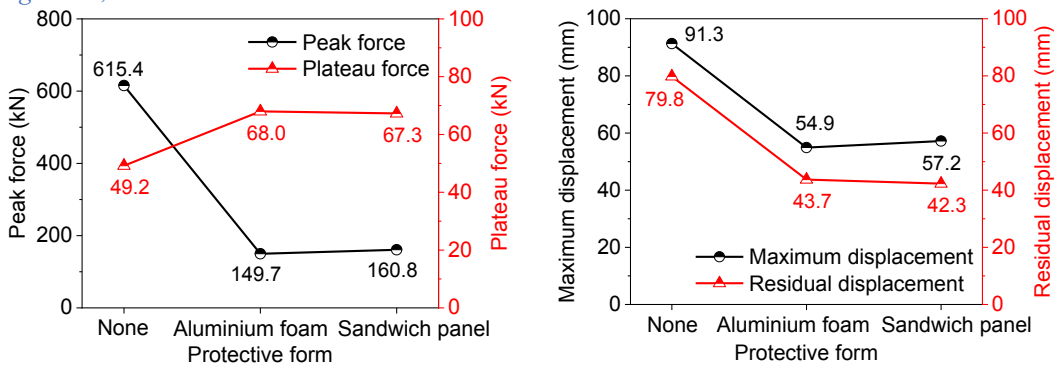

(a) Force (b) Mid-span displacement

Figure 8. Effect of protective layer type on dynamic behaviour of beams.

4. CONCLUSIONS

Impact tests were conducted on a normal reinforced concrete beam and two reinforced concrete beams with a protective layer to assess their impact resistance. The dynamic responses and failure patterns of beams with different types of protective layer were studied.

In contrast to the force-time history of the normal reinforced concrete beam, the curve of beams with a protective layer displayed a slower ascending phase of the force and a significantly lower peak force. However, the plateau force was higher, as the protective layer reduced the initial damage to the reinforced concrete beam.

Aluminium foam and sandwich panels significantly protected reinforced concrete beams by reducing the impact force and enhancing the energy absorption, causing a transformation of the failure mode from shear to flexure-shear. The utilization of aluminium foam or a sandwich panel resulted in a reduction of the maximum mid-span displacement by 39.9% and 37.3%, respectively. Furthermore, the dynamic response and failure mode observed in beams with an aluminium foam did not show apparent differences when compared to the beam protected by a sandwich panel.

ACKNOWLEDGMENTS

The authors gratefully acknowledge the financial support provided by the National Natural Science Foundation of China (Grant No.: 52278145).

REFERENCES

[1] Zhang, J., Wang, R., Han, W., & Bao, H. (2022). A comprehensive approach for bridge performance evaluation under rockfall impact integrated with geological hazard analysis. Engineering Failure Analysis, 141, 106668.

[2] Li, R. W., Wu, H., Yang, Q. T., & Wang, D. F. (2020). Vehicular impact resistance of seismic designed RC bridge piers. Engineering Structures, 220, 111015.

[3] Fujikake, K., Li, B., & Soeun3, S. (2009). Impact response of reinforced concrete beam

and its analytical evaluation. Journal of Structural Engineering, 135, 928-950.

[4] Pham, T. M., & Hao, H. (2018). Influence of global stiffness and equivalent model on prediction of impact response of RC beams. International Journal of Impact Engineering, 113, 88-97.

[5] Pham, T. M., Hao, Y., & Hao, H. (2018). Sensitivity of impact behaviour of RC beams to contact stiffness. International Journal of Impact Engineering, 112, 155-164.

[6] Zhan, T., Wang, Z., & Ning, J. (2015). Failure behaviors of reinforced concrete beams subjected to high impact loading. Engineering Failure Analysis, 56, 233-243.

[7] Zhang, S. S., Ke, Y., Smith, S. T., Zhu, H. P., & Wang, Z. L. (2021). Effect of FRP U-jackets on the behaviour of RC beams strengthened in flexure with NSM CFRP strips. Composite Structures, 256, 113095.

[8] Zhang, S. S., Yu, T., & Chen, G. M. (2017). Reinforced concrete beams strengthened in flexure with near-surface mounted (NSM) CFRP strips: Current status and research needs. Composites Part B: Engineering, 131, 30-42.

[9] Aoude, H., Dagenais, F. P., Burrell, R. P., & Saatcioglu, M. (2015). Behavior of ultra-high performance fiber reinforced concrete columns under blast loading. International Journal of Impact Engineering, 80, 185-202.

[10] Li, J., Wu, C., Hao, H., & Liu, Z. (2017). Post-blast capacity of ultra-high performance concrete columns. Engineering Structures, 134, 289-302.

[11] Nieh, T., Higashi, K., & Wadsworth, J. (2000). Effect of cell morphology on the compressive properties of open-cell aluminum foams. Materials Science and Engineering: A, 283(1-2), 105-110.

[12] Gioux, G., McCormack, T. M., & Gibson, L. J. (2000). Failure of aluminum foams under multiaxial loads. International Journal of Mechanical Sciences, 42(6), 1097-1117.

[13] Idris, M. I., Vodenitcharova, T., & Hoffman, M. (2009). Mechanical behaviour and energy absorption of closed-cell aluminium foam panels in uniaxial compression. Materials Science and Engineering: A, 517(1-2), 37-45.

[14] Schenker, A., Anteby, I., Gal, E., Kivity, Y., Nizri, E., Sadot, O., . . . Ben-Dor, G. (2008). Full-scale field tests of concrete slabs subjected to blast loads. International Journal of Impact Engineering, 35(3), 184-198.

[15] Schenker, A., Anteby, I., Nizri, E., Ostraich, B., Kivity, Y., Sadot, O., . . . Ben-Dor, G. (2005). Foam-protected reinforced concrete structures under impact experimental and numerical studies. Journal of Structural Engineering, 131(8), 1233-1242.

[16] Liu, K., Kang, S.-B., & Gao, S. (2023). Experimental and analytical study on impact response of stainless steel-aluminium foam-alloy steel sandwich panels. International Journal of Impact Engineering, 179, 104661.

[17] Zhu, F., Wang, Z., Lu, G., & Nurick, G. (2010). Some theoretical considerations on the dynamic response of sandwich structures under impulsive loading. International Journal

of Impact Engineering, 37(6), 625-637.

[18] Qi, C., Yang, S., Yang, L.-J., Wei, Z.-Y., & Lu, Z.-H. (2013). Blast resistance and multi-objective optimization of aluminum foam-cored sandwich panels. Composite Structures, 105, 45-57.

[19] CISA. (2017). Test method for room temperature compression of metallic materials. GB/T 7314-2017: Chinese Standard Press, Beijing.

[20] CISA. (2010). Metallic materials-Tensile testing-Part 1: Method of test at room temperature. GB/T 228 1-2010: Chinese Standard Press, Beijing.

"DOMINO" PROGRESSIVE FALL OF LARGE-SPAN SUSPENDED CEILING

Duozhi Wang[1], Guanglu Xu[2], Fengze Li[3], and Rong Zhang[4]

[1] Professor, Institute of Engineering Mechanics, China Earthquake Administration, wangdz@iem.ac.cn.

[2] Master student, Institute of Engineering Mechanics, China Earthquake Administration,

[3] Doctoral student, Harbin Institute of Technology.

[4] Doctor, Harbin Institute of Technology, zhangrong_hit@163.com.

Corresponding Author: Rong Zhang, Doctor.

Harbin, China.

Email: zhangrong_hit@163.com.

ABSTRACT

Progressive fall of large-span suspended ceiling occurred under only low ground motion intensity, and structure is only intact at the same time. This is a typical "Domino" progressive fall. "Domino" progressive fall needs to meet two conditions: the one is a trigger, that is, one component damages; as the other is the previous damage will lead to the next adjacent component damage, until the overall fall. The fall mechanism is verified by numerical analysis. Based on seismic investigation, the progressive fall resulted from both the insufficient anchorage between the ceiling and the structure and lacking of the lateral force bracing. Moreover, seismic design and construction of ceiling should be clarified according to seismic zones and seismic design category. Then local reinforcement is recommended to prevent the local fall from developing into a global fall.

Keywords: *large-span suspended ceiling, progressive fall, seismic investigation, non-structure.*

1. INTRODUCTION

On September 18, 2022, a Mw 6.8 earthquake struck Taiwan. The "Domino" progressive fall appeared on the large-span suspended ceiling in the badminton gym in Taoyuan City, one person was injured. Taoyuan City is more than 200 kilometers from the epicenter. According to the seismic intensity scale, the intensity is only Grade 3, the PGA is 80–250 cm/sec^2, and the PGA is 1.9 – 5.7 cm/sec, as shown in Fig 1[1,2].

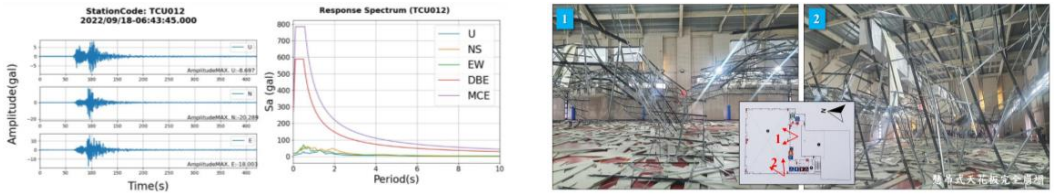

(a)The time history of ground motion (b)The response spectrum (c)The fallen ceiling

Figure 1. The basic information about earthquake[2].

Large-span suspended ceilings are usually used for important functional buildings such as airport terminals and shelters, and play a key role in the post-earthquake emergency rescue and reconstruction. Serious damage of large-span suspended ceilings usually occurred after severe earthquake both domestic and foreign severe earthquake, such as: San Francisco international airport during the Loma Prieta earthquake sequence, in 1989; Sea-Tac international airport during the Washington earthquake in 2001[3]; San Diego international airport during the Chile earthquake in 2010; the entrance hall of international airport during the Japan earthquake in 2011, etc. Moreover, In the above mentioned earthquakes, the structures were only intact or slight damaged.

Figure 2. Seismic damage of San Diego international airport.

(Chile earthquake in 2010)

Before earthquake After earthquake

Figure 3. Seismic damage of entrance hall of airport.
(Japan earthquake in 2011)

Large-span suspended ceilings used for large - span space structure which is usually a key fortification building. It is deserved to pay more attention to the whole fall of ceilings with so low ground motion intensity. In particular, the "Domino" progressive fall of large-span ceiling exposed weakness on seismic design and construction.

This paper analyzed ceiling constructions characteristic and seismic damage reason of the badminton gym in Taoyuan City. Based on the code, the "Domino" progressive fall mechanism was revealed. Moreover, the seismic measures and advises to prevent progressive fall were given out.

2. SEISMIC DAMAGE AND REASON OF LARGE-SPAN SUSPENDED CEILING

2.1. Layout of structure and ceiling

The plan view size of the badminton gym is 40 m × 26 m, and the area of the suspended ceiling is approximately 1,000 m^2. In addition to the suspended ceiling, both wind pipes and light boxes are the suspended non-structures, as shown in Fig 4. The wind pipes were under the ceiling and above the light boxes.

According to the investigation report, the vertical hanging rod is the galvanized steel runner with a C-section (38 mm × 12 mm × 1 mm, space is 900mm). The L-shaped connected piece and rivets were used to connect the hanging rod and roof; the diameter of the rivet is 4 mm and the length is 1 mm. Moreover, the main runner was connected to the bottom of the hanging rod; the main runner is also the galvanized steel runner with a C-section (38 mm × 12 mm × 1 mm, space is 1,200 mm). The cross runner was connected to the bottom of the main runner; the cross runner is the galvanized steel runner with a C-section (45 mm × 24 mm × 0.6 mm). The ceiling panel was connected with the clip on the cross runner. In addition, the panel is a perforated aluminum alloy sound absorption plate (The cross section is 300 mm × 24 mm, the length is approximately 2 m.); the perforated aluminum alloy encloses the sound absorption cotton, as shown in Fig 5[2].

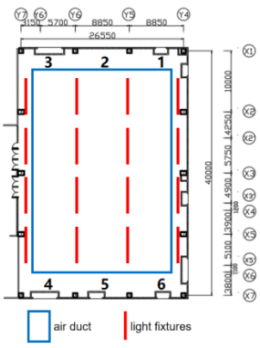

(a) Layout of badminton gym

(b) Interior view

Figure 4. The badminton gym.

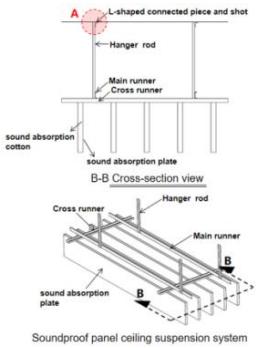

Figure 5. Layout of ceiling.

2.2. Progressive fall whole process and fall mechanism

The falling of ceiling panels began at the corner of the gym. Then the falling expanded to one side and expanded quickly from one side to the opposite side; the total time is no more than 7 s, as shown in Fig 6. This is a typical "Domino" progressive fall. "Domino" progressive fall

needs to meet two conditions: the one is a trigger, that is, one component damages; as the other is the previous damage will lead to the next adjacent component damage, until the overall fall, as shown in Fig 7.

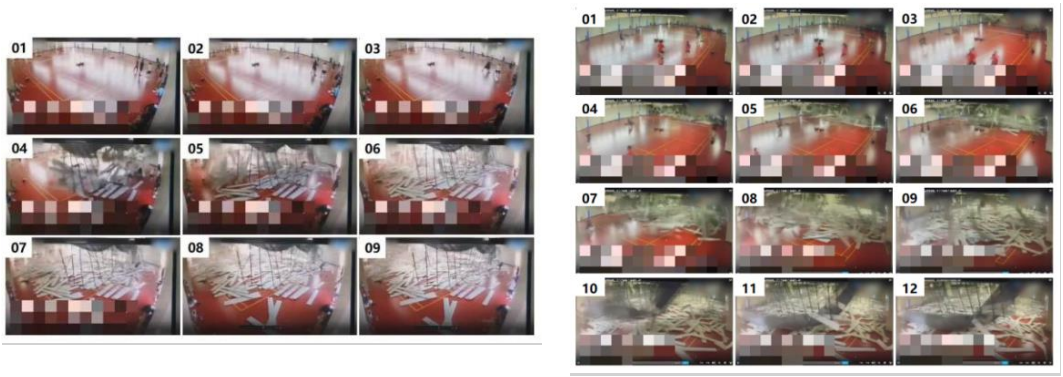

(a) Perspective 1 (b) Perspective 2

Figure 6. Progressive fall process

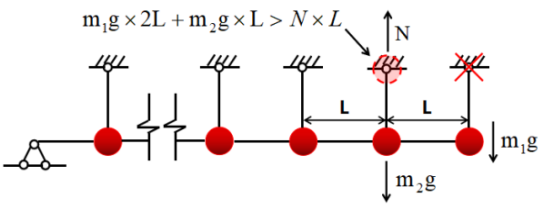

Figure 7. Progressive fall model

Many shot were pulled out, which led to connection failure between vertical hanging rod and roof. Then, the integrity of falling runner grid is good, and part of falling runner grid was on the wind pipes and light boxes that avoided the grid falling on the ground. The mass of ceiling panel is several kilograms, and panels fell from the clips during grid falling, in Fig 8. The falling at the corner is the inducement, as the weak anchoring between vertical hanging rod and roof leads to further "Domino" progressive falling.

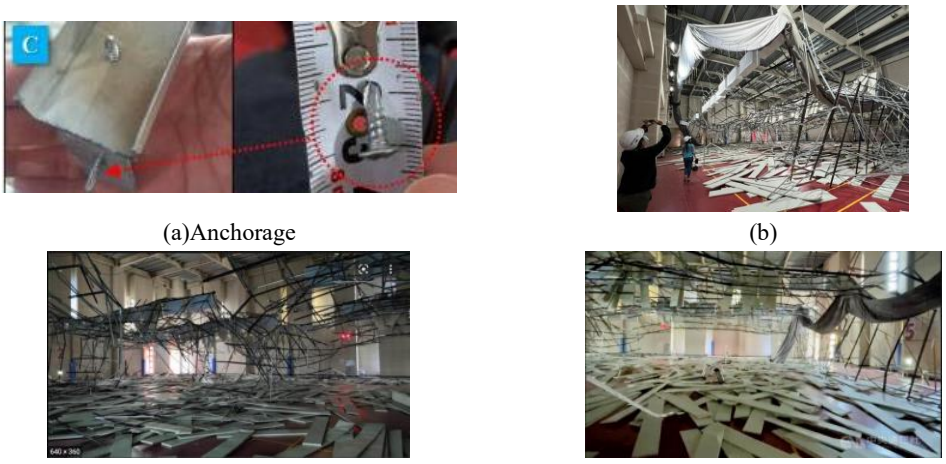

(a)Anchorage (b)

(c) (d)

Figure 8. The seismic damage

3. NUMERICAL SIMULATION

Numerical analysis is an important means to study the failure causes of non-structural components such as suspended ceiling in earthquake. It can reflect the failure process of suspended ceiling in real detail, and has the advantages of good repeatability and adjustable model parameters. In order to further analyze the cause of "Domino" progressive fall of large-span suspended ceiling in Taoyuan Badminton Hall, a simplified model of suspended ceiling was established by using finite element software ABAQUS.

The size of the simplified model is based on the actual size of suspended ceiling in the badminton stadium. The total plane size of the simplified model of the suspended ceiling is 1800mm×6000mm, and the suspension height is 900mm, which is mainly composed of the vertical hanging rod, the main runner and the cross runner. The vertical hanging rod and the main and cross runners are C-type galvanized steel, the section size and spacing are the same as above, and the B31 beam unit is used to simulate. The volume density of the commonly used sound absorption plate is 200-450kg/m³. In the model, the volume density of the sound absorption plate is 280kg/m³, and the mass points are evenly arranged in the length direction on the cross runner to simulate the load of the sound absorption plate. After simplification, each mass point is 5kg and the spacing is 400mm.

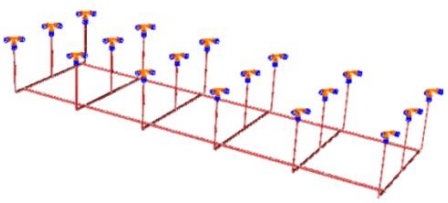

Fig 9. Finite element model

In the actual structure, the the vertical hanging rod is connected to the roof wave plate by shot. According to Technical code of cold-formed thin-wall steel structues GB50018-2002, the pulling capacity of the shot can be calculated according to the following formula:

$$N_t^f = 0.75 t_c d f \tag{1}$$

tc is the depth in which the threaded part of the nail rod is drilled into the substrate; d is the shot diameter; f is the design value of the tensile strength of the substrate. The shot is ST4.2 shot, the roof wave plate is Q345 steel, 1.5mm thick, and the design tensile strength is 300Mpa. The calculated uplift capacity is 1417.5N. The connection between the hanging rod and the roof wave plate is simulated by the CARDAN connection unit, and the calculated pulling capacity is defined as the failure load of the connection unit. In the actual earthquake damage

investigation, the connection between hanging rod, main runner and cross runner basically did not fail. The connection between them in the model adopts rigid connection. The triggering condition for the progressive fall of the ceiling system is that the hanging rod connection fails first, resulting in the failure of the adjacent hanging rod connection until the whole fall. The model is set so that the side hanging rod fails first in the earthquake.

The peak ground acceleration measured in this earthquake is 0.25g. Considering the amplification effect of building height on seismic waves, according to Code for seismic design of buildings GB50011-2010 (2016 edition) on the calculation of horizontal earthquake action of non-structural component, the position coefficient of the top of the building should be 2.0, and the bottom should be 1.0, which are distributed linearly along the height. Finally, the PFA of the input model is determined to be 0.5g, and Taft wave is selected as the external excitation for analysis. The peak acceleration in x, y and z direction of Taft wave is 0.50g, 0.44g and 0.31g, respectively.

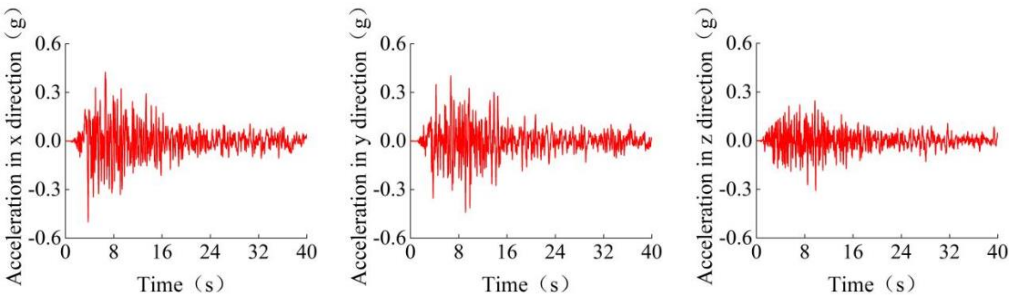

Fig 10. The acceleration time history of Taft wave

The calculation results show that the hanging rod connection at the edge of the ceiling first fails and falls (3.755s), Then the adjacent second row hanging rod falls (4.005s), and finally all the hanging rod falls (4.255s). The process of falling shows the failure mode of "Domino" progressive fall, which eventually leads to the failure and destruction of the entire ceiling system.

Consistent with the investigation of earthquake damage, when the local hanging rod fails, the adjacent components fail successively in the suspended ceiling model, which shows a progressive fall failure mode. This progressive fall mode often appears under low ground motion intensity, and eventually leads to the overall failure of the ceiling system, which is a extremely serious damage mode, and should be prevented by appropriate measures in design or construction.

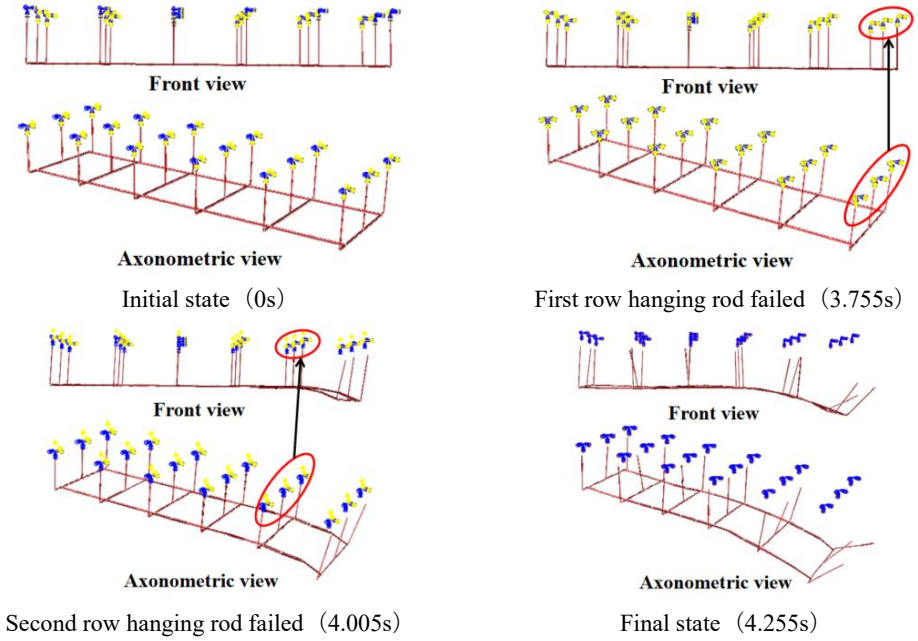

Fig 11. Progressive fall process of suspended ceiling

4. LARGE-SPAN CEILING SEISMIC CODE REQUIREMENTS

According to Taiwan code, the lateral force bracing was required for all ceiling areas greater than 93 ㎡, and seismic separation joints were required for all ceiling areas greater than 250 ㎡. In addition to ASTM C635 and ASTM C636, the code should refer to ASTM-E580 for the high seismic zone[4-6].

The area of Badminton gym is more than 1000 ㎡, then no lateral force bracing was found during seismic investigation.

Moreover, the shot which used for connecting structure and ceiling, can't meet with anchorage requirement. The shot is no more than 1.5 cm (Fig. 8 (a)), the required anchorage length is more than 0.75" (1.90 cm) as listed in CISCA[7-8].

5. CONCLUSION AND RECOMMENDATIONS

The "Domino" progressive fall appeared on the large-span suspended ceiling in the badminton gym under low ground motion intensity, while structure was only intact during Mw 6.8 Taiwan earthquake in 2022. The main reasons are 1. Insufficient anchorage between the ceiling and the structure; 2. The lateral force bracing was not found.

Through theoretical analysis and numerical simulation of the failure process of the suspended ceiling, it is found that the suspended ceiling may fall continuously under low ground motion intensity, which seriously affects the function of the building and even causes casualties. Therefore, seismic design and construction of ceiling should be clarified according to seismic zones and seismic design category. The anchoring between suspended ceiling and structure

need to be enhanced and evaluated. Then local reinforcement is recommended, which prevents the local fall from developing into a global fall. Finally, the anchoring of heavy ceiling panel needed to be enhanced and evaluated.

ACKNOWLEDGEMENTS

Greatest gratitude of authors goes to the financial support from the National Key Research and Development Plan, China (2019YFE0112700), and special thanks are also due to Professor Zhaozhi YAO for fruitful discussions of and help with this paper.

REFERENCES

[1] Meteorological Bureau Seismic Intensity Scale.

[2] ZHOU Zhongzhe, WU Junlin, CHAI Junfu, YAO Zhaozhi. (2022). 2022 Taiwan Guanshan earthquake and Chishang earthquake survey disaster report.

[3] Kawaguchi , Ken'ichi.(2012). Structures Congress 2012 Proceedings of the 2012 Structures Congress, 2012: 1035-1044.

[4] C635 Specification for the Manufacture,Performance,and Testing of Metal Suspension Systems for Acoustical Tileand Lay-in Panel Ceilings.

[5] C636 Practice for Installation of Metal Ceiling SuspensionSystems for Acoustical Tile and Lay-In Panels.

[6] ASTM E580/E580M-11b*1 Standard Practice forInstallation of Ceiling Suspension Systems for AcousticalTile and Lay-in Panels in Areas Subject to EarthquakeGround Motions1.

[7] Ceiling and Interior System Construction Association, Guidelines for Seismic Restraint Direct Hung Acoustical Suspended Ceiling Assemblies Seismic Zones 3 & 4, 2004

[8] Ceiling and Interior System Construction Association, Recommendations for Direct Hung Acoustical Tile and Lay-In Panel Ceilings Seismic Zones 0-2, 2004

APPLICATION OF CO_2 MINERALISED CONCRETE TO REDUCE EMBODIED CARBON FOR A SUSTAINABLE BUILT ENVIRONMENT IN SINGAPORE

Wang Su[1], Anne Thymotie[2], Kwek Shi Ying[3], Yap Zhen Shyong[4]

[1] Senior Scientist, Pan-United Corporation Ltd, su.wang@panunited.com.sg

[2] Scientist, Pan-United Corporation Ltd, anne.thymotie@panunited.com.sg

[3] Scientist, Pan-United Corporation Ltd, E-mail address, shiying.kwek@panunited.com.sg

[4] Scientist, Pan-United Corporation Ltd, zhenshyong.yap@panunited.com.sg

Corresponding Author: Wang Su, PhD, MSc.

12 Kaki Bukit Crescent, Singapore, 416243

Email: su.wang@panunited.com.sg

ABSTRACT

This paper explores the application of CO_2 mineralised concrete produced by Pan-United Corporation Ltd as a sustainable building material in the context of Singapore's urban environment. Traditional concrete production is a significant contributor to CO_2 emissions, prompting the need for environmentally-friendly alternatives. CO_2 mineralised concrete, which is an application of Carbon Capture and Utilisation (CCU) technology in the concrete industry, offers a promising solution by achieving carbon mineralisation during the fresh concrete mixing. The study assesses the feasibility, performance and environmental impact of incorporating this innovative building material as a construction practice in Singapore. The research investigates the fresh property, mechanical properties and durability of CO_2 mineralised concrete, which shows comparable or even better performance than reference normal concrete. Furthermore, the paper discusses the environmental analysis associated with the adoption of this technology in the local construction industry, exhibiting its potential to enhance the sustainability of the built environment. The findings contribute to the ongoing global effort to reduce the carbon footprint of infrastructure development and promote a more sustainable and resilient urban landscape.

Keywords: *CO_2 mineralisation, workability, strength, durability, embodied carbon, EPD*

1 INTRODUCTION

Anthropogenic activities have increased the global CO_2 concentration from 270 to 350 ppm since 1700 and are expected to increase to 500 ppm by 2050 [1]. Singapore, due to its rapid urbanization and construction boom, has also encountered unprecedented challenges in terms of carbon emissions, particularly concerning the carbon footprint associated with the construction industry. In this regard, the Singapore Green Plan 2030 has committed to reduce emissions to around 60 $MtCO_{2e}$ in 2030 after peaking emissions earlier, and to achieve net zero emissions by 2050. The carbon emissions from building construction consist of two components: embodied and operational carbon. Operational carbon refers to the carbon emissions of a building or structure when it is in use, such as lighting and air conditioning. Embodied carbon refers to the carbon emissions from the manufacturing and transportation of all the materials needed to construct the building. Simply put, embodied carbon refers to the carbon footprint of a building or structure before it is completed and in use. With the development of energy-efficient technology and innovation, operational carbon can be managed and reduced. Hence, the embodied carbon factor continues to grow in importance as a proportion of total emissions. Most importantly, unlike operational carbon, embodied carbon cannot be mitigated after the building or structure is completed, and such emission are irreversible.

Cement and concrete are the most widely used construction materials and are estimated to account for about 8% of annual global CO_2 emissions. Lowering the carbon footprint of both materials can effectively reduce embodied carbon emissions in the construction industry. As a global leader in low-carbon concrete technologies, Pan-United Corporation is committed to decarbonising the built environment with its sustainable concrete products and technologies. Its flagship PanU CO_2 Mineralised Concrete uses innovative CCU technology to make stronger and greener concrete with industrially-emitted recycled carbon dioxide. The CO_2 serves as a type of raw material that is injected into a central mixer during fresh concrete mixing; this CO_2 reacts with cement clinker in the presence of water. The main chemical reaction is shown as follows [2]:

$$C_3S + (3-x)CO_2 + yH_2O \rightarrow C_xSH_y + (3-x)CaCO_3 \quad (1)$$

$$C_2S + (2-x)CO_2 + yH_2O \rightarrow C_xSH_y + (2-x)CaCO_3 \quad (2)$$

The injection process mineralises the CO_2 very quickly under normal conditions [3], generating nanoscale and interconnected calcium silicate hydrates (C-S-H) gel and calcium carbonate ($CaCO_3$). Both carbonated products are beneficial to the strength and durability of the resulting concrete, while allowing for less cement content in the concrete mix design - which further reduces the carbon footprint. The CCU technology has been industrialised for RMC production where CO_2 effectively becomes an admixture in fresh concrete during the batching and mixing process. A vessel with CO_2 in liquid form is installed beside the central mixer and an accurate

and optimised dosage of CO_2 is measured and injected into the central mixer by a control system portion.

This paper reports the performance of different grades of CO_2 mineralised concrete produced in a Pan-United batching plant and compares with reference normal concrete in terms of workability, strength and durability. In addition, the environmental impact of PanU CO_2 mineralised concrete versus reference normal concrete is quantified and compared to illustrate the environmental benefits of adopting this sustainable Pan-United concrete and technology.

2 MATERIALS AND METHODS

2.1 Raw material and mix design

Three sets of PanU CO_2 mineralised concrete (G20_CO_2, G40_CO_2, G60_CO_2) and three sets of corresponding reference normal concrete (G20, G40, G60) were prepared at a Pan-United batching plant in Tuas. The mix design of the total six sets of samples are listed in Table 1.

Table 1 Mix design of G20, G20_CO_2, G40, G40_CO_2, G60 and G60_CO_2

Raw materials	G20	G20_CO_2	G40	G40_CO_2	G60	G60_CO_2
Cement (kg/m^3)	305	290	440	420	550	520
Coarse aggregate (kg/m^3)	1015	1015	950	950	980	980
Fine aggregates (kg/m^3)	670	685	735	750	675	700
Water (kg/m^3)	189	189	198	198	172	172
Retarder (L/m^3)	1.22	1.16	2.20	2.10	2.75	2.75
Superplasticizer (L/m^3)	1.07	1.02	1.98	1.89	4.13	4.13
CO_2 (kg/m^3)	0	0.44	0	0.63	0	0.83
Water-to-cement ratio	0.62	0.65	0.45	0.47	0.31	0.33

The cement used in the current study is Ordinary Portland Cement CEM I, 42.5 N. The coarse and fine aggregates have fineness modulus of 5.8 and 3.5, respectively. The CO_2 stored and used in the batching plant is the by-product of refineries at Jurong Island, Singapore. It should be noted that the cement content in PanU CO_2 mineralised concrete was 5% less than the corresponding reference concrete and hence the water-to-cement ratio of CO_2 mineralised concrete was slightly higher than the corresponding reference concrete.

2.2 Testing methods

Table 2 summarises the testing programme of CO_2 mineralised concrete and the corresponding reference concrete in terms of workability, strength and durability. All the testing samples for each mix design were cast by the 3 m^3 of fresh concrete batched and mixed at the plant following the standard process. The samples were demoulded and cured according to the

requirements in standards for various tests as listed in Table 2. At least three same samples were prepared for each test and the average results were presented.

Table 2 Testing programme of G20, G20_CO_2, G40, G40_CO_2, G60 and G60_CO_2

Property category		Method	Standard
Fresh properties	Workability	Slump test	BS 12350-2:2019 [4]
Mechanical properties	Compressive strength	Compression test	BS EN 12390 3:2019 [5]
Durability	Permeability	Water penetration test	BS EN 12390-8:2019 [6]
	Diffusivity	Rapid chloride migration test	NT BUILD 492 [7]
	Carbonation	Accelerated carbonation test	BS 1881-Part 210:2013 [8]

3 Results and discussion

3.1 Workability

The workability of the fresh concrete onsite was evaluated by slump testing according to BS 12350-2:2019 [4] and the results are shown in Figure 1. It was found that the initial slump results of PanU CO_2 mineralised concrete (G20_CO_2, G40_CO_2, G60_CO_2) are almost the same as the corresponding reference concrete (G20, G40, G60). This indicates that the introduction of CO_2 during the fresh concrete mixing process have minimum impact on the workability.

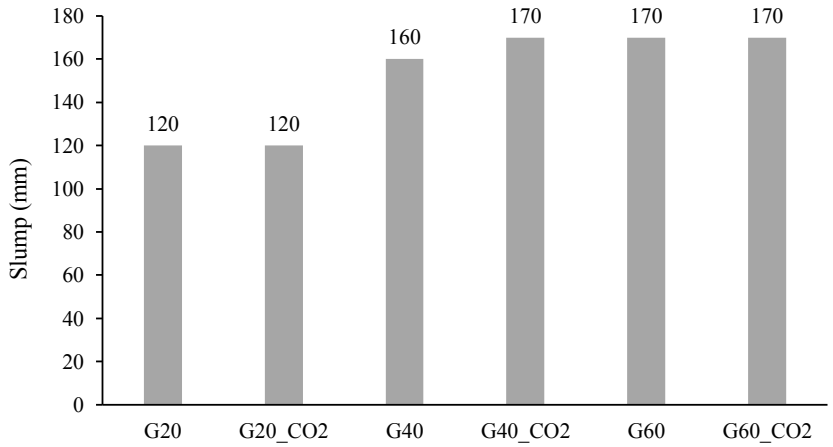

Figure 1 Initial slump testing results of G20, G20_CO_2, G40, G40_CO_2, G60 and G60_CO_2

3.2 Compressive strength

The 1-day and 28-day compressive strengths of samples in the current study were tested on 150 mm cubes in accordance with BS EN 12390-3:2019 [5]. Figure 2 illustrates that all the PanU CO_2 mineralised concrete (G20_CO_2, G40_CO_2, G60_CO_2) and corresponding reference

concrete (G20, G40, G60) achieved the designed 28-day compressive strength. More importantly, both the 1-day and 28-day compressive strengths of PanU CO_2 mineralised concrete were comparable or even slightly higher than the corresponding reference concrete, although the cement volume in PanU CO_2 mineralised concrete was 5% lower than that of the corresponding reference concrete. This is attributed to the nucleation effect of the nano-sized calcium carbonate formed during the CO_2 mineralisation process (Equation 1 and 2) to accelerate the hydration process, resulting in more homogenous hydration products and less porous microstructures. This result corresponds with the previous study [3] where the CO_2 injected during mixing improved the compressive strength and cement usage efficiency of the concrete.

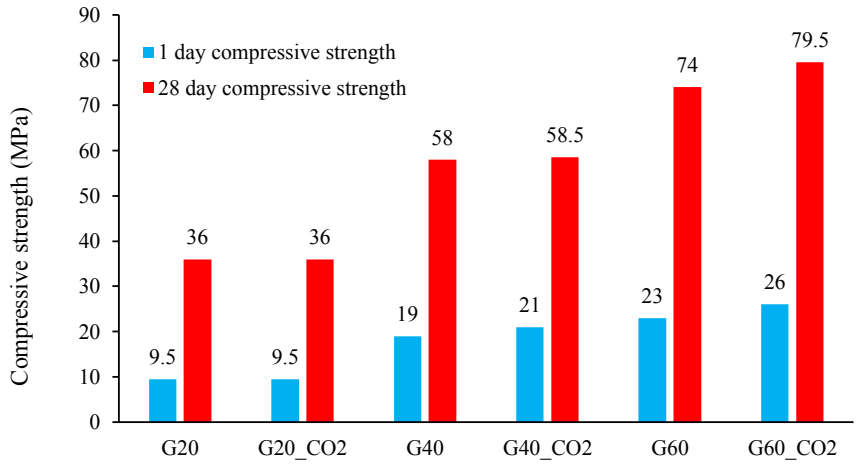

Figure 2 Compressive strength of G20, G20_CO_2, G40, G40_CO_2, G60 and G60_CO_2

3.3 Durability

The durability in this study is evaluated by permeability (water penetration), diffusivity (rapid chloride migration) and carbonation (accelerated carbonation tests) as presented in Figure 3, Figure 4 and Figure 5. Water penetration tests were conducted on 150 mm cubes at the 28-day curing age following BS EN 12390-8:2019 [6] while the rapid chloride migration tests were conducted on $\emptyset 100 \times 50$ mm disks at the 28-day curing age following NT BUILD 492 [7]. The results from Figure 3 and Figure 4 gave similar conclusions that the PanU CO_2 mineralised concrete (G20_CO_2, G40_CO_2, G60_CO_2) had comparable or even lower permeability and diffusivity than the corresponding reference concrete (G20, G40, G60). Like the explanation for improved compressive strength, the reduced porosity from CO_2 mineralisation technology can reduce the transport properties.

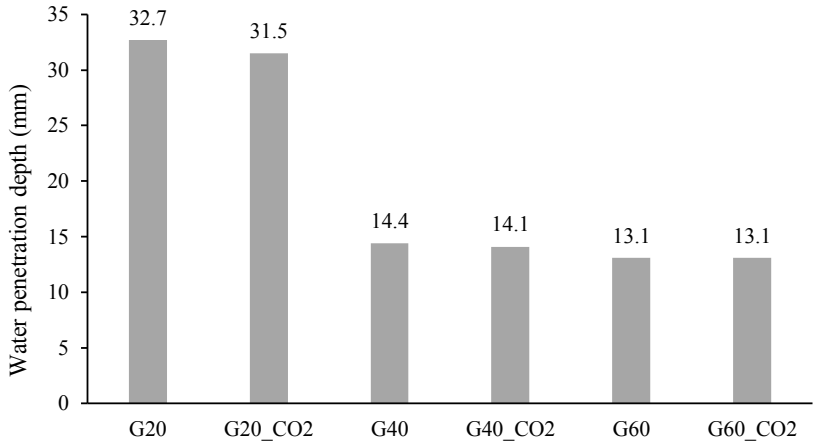

Figure 3 Water penetration depth of G20, G20_CO2, G40, G40_CO2, G60 and G60_CO2

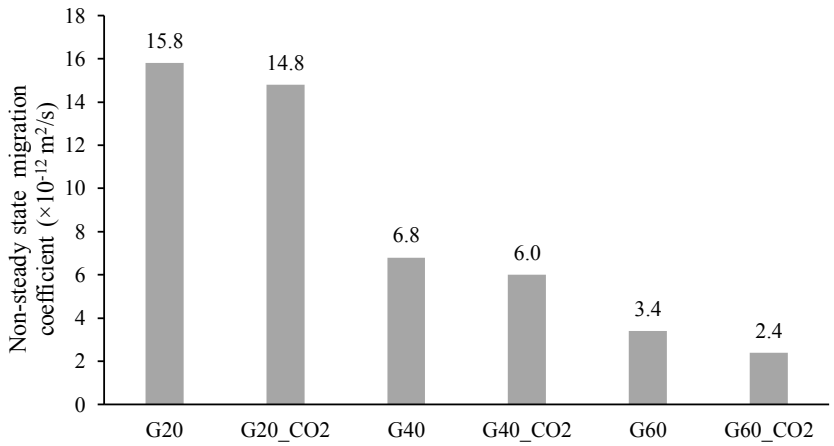

Figure 4 Chloride diffusivity of G20, G20_CO_2, G40, G40_CO_2, G60 and G60_CO_2

The accelerated carbonation tests were conducted on 150 mm cubes at the exposure ages of 28, 42 and 56 days according to BS 1881-Part 210:2013 [8]. The accelerated carbonation depth was plotted in Figure 5 as a function of the exposure age. It can be found that the accelerated carbonation depth was reduced with the increased concrete grade due to the denser microstructure with increasing concrete strength.

The carbonation of PanU CO_2 mineralised concrete is always a concern for customers because it seems that the addition of CO_2 can increase concrete carbonation and cause corrosion in the embedded steel reinforcement. However, Figure 5 shows that the PanU CO_2 mineralised concrete (G20_CO_2, G40_CO_2, G60_CO_2) showed quite similar or even slightly lower accelerated carbonation depth compared with the corresponding reference concrete (G20, G40, G60).

Firstly, the CO_2 mineralisation technology can densify the matrix microstructure so that the diffusion of CO_2 from the atmosphere into the hardened concrete pores can be reduced. Secondly, the CO_2 mineralisation occurs at the very beginning of cement hydration, i.e. the initial hydrolysis and induction period. Therefore, as shown in Equations 1 and 2, injected CO_2 reacts with calcium ions dissolved from the cement clinker [2, 3] but not the calcium hydroxide, which is one of the hydration products, so that the pH value of the pore solution in hardened concrete will not be influenced.

Generally, over its long-term service life, PanU CO_2 mineralised concrete has at least comparable or even less carbonation depth or risk of rebar corrosion than the reference normal concrete when exposed to the same environment.

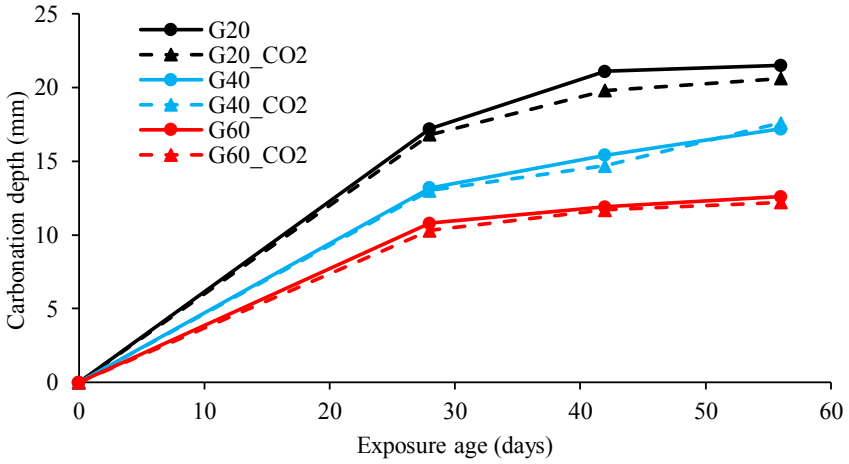

Figure 5 Accelerated carbonation depth of G20, G20_CO_2, G40, G40_CO_2, G60 and G60_CO_2

4 Environmental analysis

In December 2022, Pan-United became the first concrete company in Asia to provide on-demand Environmental Product Declaration certificates (EPDs). An EPD is a third-party verified report disclosing the environmental impact of a specific product based on an entire life cycle assessment. It represents the product's "climate change total" quantified in terms of "$kgCO_{2e}$" (kilogramme equivalent of carbon dioxide).

The EPDs for Pan-United's concrete mix designs are independently audited in accordance with BS EN ISO 14025 [9] and BS EN 15804+A2 [10]. An example is given here to compare the quantified environmental impact calculated by EPDs between G40 PanU Green CO_2 Mineralised Concrete and the corresponding G40 reference normal concrete. The mix designs and EPD results are showed in Table 3 and Table 4.

Table 3 Mix design of PanU Green CO_2 Mineralised Concrete and corresponding reference concrete

Raw materials	PanU Green CO_2 Mineralised Concrete	Reference normal concrete
Grade	40	40
Cement (kg/m^3)	273	410
Slag (kg/m^3)	117	0
Coarse aggregate (kg/m^3)	1000	1000
Fine aggregates (kg/m^3)	765	735
Water (kg/m^3)	185	185
Retarder (L/m^3)	1.56	2.05
Superplasticizer (L/m^3)	2.34	1.64
CO_2 (kg/m^3)	0.585	0

Table 4 EPDs' results of PanU Green CO_2 Mineralised Concrete and corresponding reference concrete

Environmental data	PanU Green CO_2 Mineralised Concrete	Reference normal concrete	Reduction (%)
Climate Change-total (kg CO_2eq)	290	398	27.1
Ozone Depletion (kg CFC-11-eq)	9.82×10^{-6}	1.05×10^{-5}	6.5
Acidification (mol H^+eq)	1.12	1.34	16.4
Eutrophication-freshwater (kg PO_4eq)	0.04	0.05	20.0
Eutrophication-marine (kgN eq)	0.26	0.32	18.8
Eutrophication-terrestrial (mol N eq)	2.83	3.55	20.3
Abiotic Depletion-minerals, metals (Kg Sb eq)	1.36×10^{-5}	1.38×10^{-5}	1.4
Abiotic Depletion-fossil (MJ)	1532	1775	13.7

Note: the above data was calculated based on 1 m^3 of concrete

Compared to the G40 reference normal concrete in Table 3, PanU G40 Green CO_2 Mineralised Concrete utilised 30% slag to replace the cement and employed the CO_2 mineralised technology together with 5% binder reduction. With the joint efforts of the above two sustainable approaches, all the environmental impact data are reduced, especially the Climate Change-total (kg CO_2eq) - which represents the global warming potential - is reduced by 27.1%. Singapore's carbon tax level for the first five years (2019-2023) was set at S$5/t$CO_{2e}$ to provide a transitional period for emitters to adjust. However, the carbon tax was increased to S$25/t$CO_{2e}$ starting in 2024 to promote the net zero target. It is scheduled to rise further to S$45/t$CO_{2e}$ for the years of 2026 and 2027, with a view to reaching S$50-80/t$CO_{2e}$ by 2030. Therefore, the developers' savings of carbon tax will be more and more significant by using the green CO_2 mineralised concrete.

The provision of verifiable and audited environmental data empowers developers to lower the embodied carbon footprint of their projects and strengthens efforts to green the built environment. These EPDs not only build greater confidence in our green concrete products but are also significant in advancing the built environment towards net zero.

5 Conclusion

This paper discussed the comparison between CO_2 mineralised concrete produced by Pan-United and reference normal concrete in terms of their engineering properties and environmental impact. Generally, the fresh and hardened properties of CO_2 mineralised concrete were comparable or resulted in even better performance than the reference normal concrete.

Most importantly, the injected CO_2 is chemically converted into nano-CaCO3 minerals and embedded in concrete permanently. The EPD results show that CO_2 mineralised technology can stack on with other low-carbon technologies to significantly reduce the embodied carbon footprint of concrete.

Such quantified and verified environmental impact data represent a significant step forward in enhancing sustainability transparency in the concrete industry and empowers the consumers, businesses and policymakers to make environmentally-conscious choices.

REFERENCES

[1] Intergovernmental Panel on Climate Change, IPCC)

[2] Berger, R. L., Young, J. F., & Leung, K. J. N. P. S. (1972). Acceleration of hydration of calcium silicates by carbon dioxide treatment. Nature Physical Science, 240(97), 16-18.

[3] Monkman, S., Lee, B. E., Grandfield, K., MacDonald, M., & Raki, L. (2020). The impacts of in-situ carbonate seeding on the early hydration of tricalcium silicate. Cement and Concrete Research, 136, 106179.

[4] BS EN 12350-2: 2019 (2019), Testing fresh concrete - Part 2: Slump test, Brussels, Belgium.

[5] BS EN 12390-3: 2009 (2009), Testing hardened concrete - Part 3: Compressive strength of test specimens, Brussels, Belgium.

[6] BS EN 12390-8: 2009 (2009), Testing hardened concrete - Part 8: Depth of penetration of water under pressure, Brussels, Belgium.

[7] NT Build 492 (1999), Concrete Mortar and Cement-based Repair Materials: Chloride Migration Coefficient from Non-stead-state Migration Experiments, Nordtest, Esbo, Finland.

[8] BS 1881-210:2013 (2013), Testing hardened concrete Part 210: Determination of the potential carbonation resistance of concrete – Accelerated carbonation method, British Standards: London, UK.

[9] BS EN ISO 14025:2010 (2010), Environmental labels and declarations — Type III environmental declarations — Principles and procedures, Brussels, Belgium.

[10] BS EN 15804:2012+A2: 2019 (2019), Sustainability of construction works – Environmental product declarations – Core rules for the product category of construction products, Brussels, Belgium.

DISASTERS SUCH AS ROCKFALLS DURING THE NOTO PENINSULA EARTHQUAKE

Hiroshi Masuya [1], Michiaki Yamamoto[2], Yoichi Nishita[3], and Yusuke Kurihashi[4]

[1] Doctor of Engineering, Protech Engineering Co., Ltd., masuya@proteng.co.jp.

[2] Ph.D. (Engineering), Protech Engineering Co., Ltd., yamamoto@proteng.co.jp.

[3] Ph.D. (Engineering), Protech Engineering Co., Ltd., nishita@proteng.co.jp.

[4] Professor, Kanazawa University, kuri@se.kanazawa-u.ac.jp.

Corresponding Author: Hiroshi Masuya, Doctor of Engineering, Technical advisor

1-442 Takaodai, Kanazawa, Ishikawa Prefecture, Japan, Postal code 921-8155

Email: masuya@proteng.co.jp

ABSTRACT

Just after 2:30 pm on May 5, 2023, a magnitude 6.5 earthquake occurred in the Noto region of Ishikawa Prefecture. Tremors with a seismic intensity of 6+ were observed in Suzu City, Ishikawa Prefecture. As a result of this earthquake, a 10 cm tsunami was observed at Wajima Port. Landslides such as rockfalls have also occurred on the Noto Peninsula, and the presence of unstable rock masses on the slopes raised the possibility of new rockfalls. Then, just after 4 p.m. on January 1, 2024, a large earthquake with a magnitude of 7.6 occurred. In Wajima City, Ishikawa Prefecture, tremors with a seismic intensity of 7 were observed, causing severe damage. The earthquake also caused a tsunami of more than 4 meters in height, causing damage. In this paper, the damage caused by the Noto Peninsula Earthquake are reported in detail and the effects of protective measures and future protective facilities are discussed.

Keywords: *rockfall, earthquake, slope disaster, Tsunami, liquefaction phenomenon, Damage to structures.*

1. INTRODUCTION

In the Noto region of Ishikawa Prefecture, the number of earthquakes has been increasing since around 2018, and seismic activity has increased since December 2020[1]. According to the Japan Meteorological Agency, since December 2020, tremors with a seismic intensity of 1 or higher have been observed 437 times as of 8:00 a.m. on June 8, 2023[2]. Just after 2:30 p.m. on May 5, 2023, an earthquake with a magnitude of 6.5 occurred with its epicenter at a depth of 12 km in the Noto region of Ishikawa Prefecture, and shaking with a magnitude of 6+ was observed in Suzu City, Ishikawa Prefecture. As a result of this earthquake, a 10 cm tsunami was observed at Wajima Port and a 4 cm tsunami was observed at Suzu Nagabashi. This

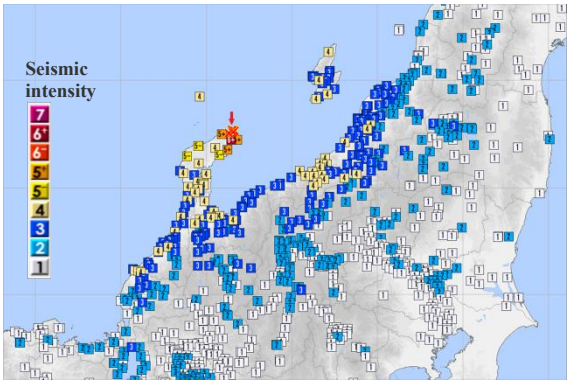

Figure 1. Epicenter and seismic intensity distribution of Oku Noto Earthquake (May 5, 2023)

earthquake was followed by a series of earthquakes in the Noto region that made you feel the tremors in your body, followed by rain that lasted until the 7th, and landslides. The earthquake that occurred on May 5, 2023 and caused damage was named the ``2023 (Reiwa 5) Oku-Noto Earthquake'' by Ishikawa Prefecture. In this paper, firstly the report has been done on the damage caused by the Oku-Noto earthquake and slope disasters such as rockfalls.

Seven months after the Oku-Noto earthquake, a new major earthquake with a magnitude of 7.6 occurred at around 4:10 pm on January 1st, with the epicenter at a depth of 16 km in the Noto region of Ishikawa Prefecture. As a result of this earthquake, extremely violent shaking with a seismic intensity of 7 was observed in Shiga and Wajima, as well as seismic intensity 6 upper in Nanao, Suzu, and Anamizu, and seismic intensity 6 lower was observed in Nakanoto, Noto, Niigata Nagaoka. Significant damage occurred in areas where high seismic intensity was observed.

The magnitude of the earthquake that caused the Great Hanshin-Awaji Earthquake and the Kumamoto Earthquake was 7.3, so it was larger than those. According to the Japan Meteorological Agency, this is the first time in the history of observation that a magnitude 7 earthquake has been observed in Ishikawa Prefecture. The Japan Meteorological Agency has named this series of seismic activity the “2024 (Reiwa 6) Noto Peninsula Earthquake”. Since then, earthquakes have continued to occur one after another, with over 1,500 earthquakes with a seismic intensity of 1 or higher observed in the month since the January 1st earthquake. In this paper, following on the Oku-Noto earthquake, the report in detail about the Noto Peninsula earthquake has been done.

2. OKU-NOTO EARTHQUAKE

2.1. Overview of Oku-Noto earthquake

Figure 1. shows the epicenter of the magnitude 6.5 earthquake with the seismic intensity distribution of earthquake that occurred at a depth of 12 km in the Noto region of Ishikawa

Table.1 Name of the observation station with Japanese seismic intensity of 4 or higher

Seismic intensity	Province	Observer name
6 upper	Ishikawa	Shoin Suzu
5 upper	Ishikawa	Misaki Suzu, Otani Suzu, Matsunami Noto
4	Ishikawa	Fugeshi Wajima, Hasiride Monzen, Usitu Noto
4	Ishikawa	Sainen Kanazawa, Futyu-machi & Sodegae-machi & Kakiyoshi-machi & Notojima Mukaida-machi Nanao, Komade-machi Komatsu, Hegura island & Kawai-machi Wajima, Asahi-machi Hakui, Hamakita Kahoku, Raimaru-machi Nomi, Togiryoke & Sueyosisenko Sika-machi, Suesaka & Notobeshimo Nakanoto-machi, Omachi Anamizu, Yanagida Noto-machi
4	Niigata	Nakanoshima Nagaoka, Shinbori Sanjo, Chitose-machi & Matsunoyama, Tokamachi, Tamachi Myoko, Nakanomata & Otemachi & Kida & Maki-ku-Yanagishima, Kakizaki-ku-Kakizaki, Ogata-ku-Dosokohama, Kibiki-ku-Hyaken-machi, Yoshikawa-ku-Harano-machi, Sanwa-ku,-Inoguchi, Itakura-ku,-Hari, Natachi-ku-Natachiomachi Jyouetsu, Iwataniguchi & Kawaradahonmachi & Akadomari & Ogimachi Sado, Warimachishinden Kariwa
4	Toyama	Fukuoka Takaoka, Kano Himi, Izumi-machi Oyabe, Kojima& Honmachi, Hashimotojo & Futakuchi & Kamo Chubu Oyabe, Bussyouji Funabashi-mura
4	Fukui	Itihime & Kunikage Awara, Mikuni-machi Tyuou Sakai

Table2. Damage situation of Oku-Noto earhtquake (human damage/building damage)

City			Kanazawa	Wajima	Suzu	Noto	Total
Human casualties	Dead person				1		1
	Missing person						
	Injured person	Serious wound			2		2
		Minor injury			30	1	31
Damage to houses	Complete destruction				9		9
	Half destruction				9		9
	Partially damaged		1	1	450		450
	Flooding above the floor						
	Flooding under the floor						
Damage to non-residential houses	Public Buildings						
	Others				36		36

Prefecture, which occurred just after 2:30 p.m. on May 5, 2023 [3]. Maximum seismic intensity of 5+ observed in Suzu, and a long-period ground motion class 2 observed in Noto, Ishikawa Prefecture. **Table 1.** shows observation points where seismic intensity 4 or higher was observed [4]. It can be seen that strong shaking was observed in a wide range of areas other than Ishikawa Prefecture, including Niigata Prefecture, Toyama Prefecture, Fukui Prefecture, and the Hokuriku region.

Table 2. shows a list of major earthquake damage situations. In Suzu, a man in his 60s died after falling from a ladder [5]. In the city, water was cut off for 39 households, and tap water became cloudy in some areas, but this had all been resolved by May 7th. National Route 249

Gravestone

Entrance of a shopping center

Figure 2. Damage to gravestone and entrance of a shopping center caused by the earthquake

was temporarily closed in two places in Suzu and Wajima due to falling rocks and expanding cracks in the road surface caused by the earthquake, but emergency restoration work was carried out and alternate traffic on one side was possible by May 10.

2.2. Damage caused by Oku-Noto earthquake

Naturally, the greatest damage occurred in areas with high seismic intensity, as shown in **Figure 1**. **Figure 2.** shows the damage to gravestone in Suzu and the damage to the block pavement at the entrance to a shopping center near Iida Port which were caused by the earthquake (intensity 6+) . The shopping center was built on reclaimed land, so the shaking was likely strong. The cracks in the ground were observed at the Iida Elementary School playground caused by the earthquake. In addition, cracks were observed in the exterior asphalt, but there was no major damage to the building. At Noto High School, water leaks and cracks in the walls were reported due to cracks in the boiler room drainage pipe, and at Iida High School, cracks in the gymnasium aisles, falling concrete pieces, and water leaks were reported [6]. **Figure 3.** shows a house that collapsed due to the earthquake(intensity 6+). **Figure 4.** shows Mitsuke Island where the collapse was observed (intensity 6+). **Figure 5.** (intensity 5+) show Yaseno cave gate (Yasenodomon, National Route 249). The old tunnel was damaged due to the Noto Peninsula Earthquake in 2007, and one side of the tunnel was closed to traffic

Figure 3. Collapsed houses in Suzu

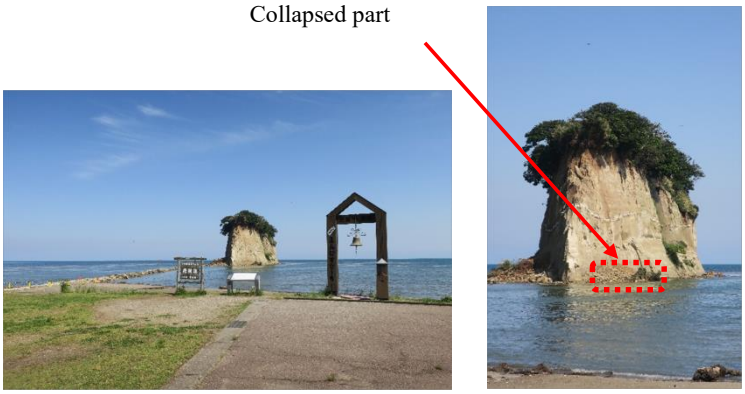

Figure 4. Mitsuke island in Suzu (also known as Warship island) where the collapse was seen

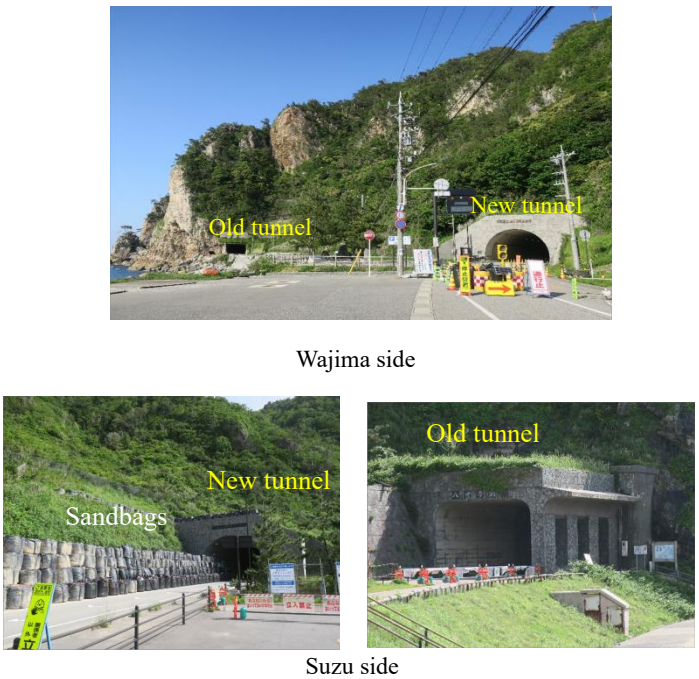

Figure 5. Yaseno cave gate

alternately and at night. It is known that unstable rock masses exist over a wide area along this coastline, making it dangerous. In 2009, this new tunnel with a length of 722 meters connecting Sosogi in Wajima and Maura in Suzu was opened to traffic. However, as shown in the new tunnel in **Figure 5.**, there are still unstable rock masses, which are protected by many heavy sandbags.

Figure 6. shows the destruction of the rockfall protection net and the source of the rockfall that occurred after the heavy rains on June 2nd, although not during the earthquake. It is assumed that the rockfall occurred because a large amount of rain fell on the slope loosened by the earthquake. Rockfall protection fences along roads were also destroyed during rockfalls. On June 3rd, falling rocks were removed from the road shoulder to allow one-way traffic, but the road was closed due to the fear of secondary disasters caused by falling rocks. After that, the

source rockfall and the unstable rockfall. Although the work was carried out on a steep slope, all of the debris was crushed and removed, making it passable.

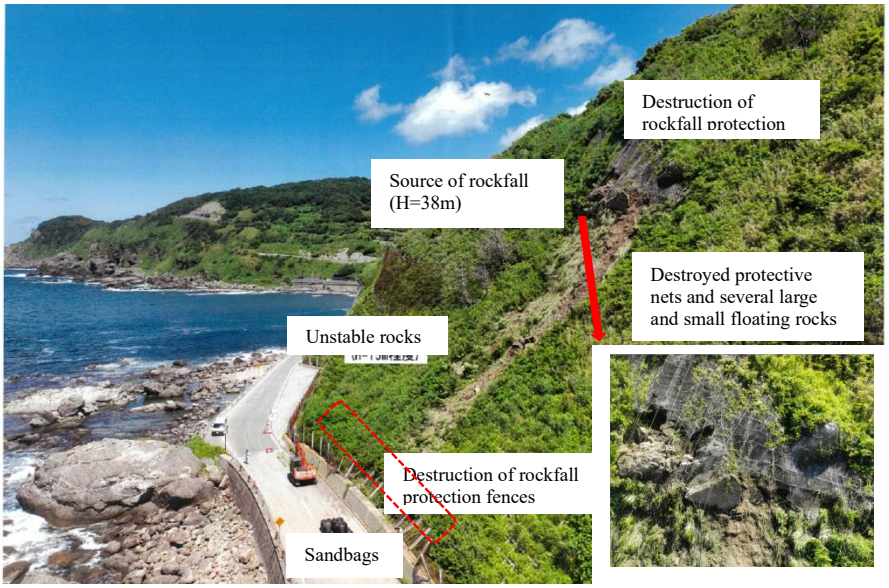

Figure 6. Rockfall source (Osawa Wajima)

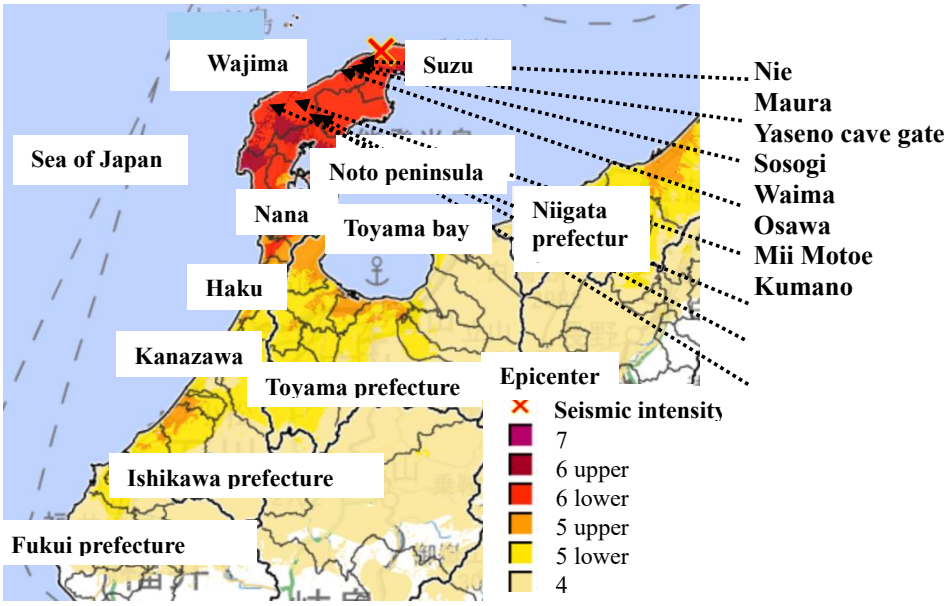

Figure 7. Epicenter and seismic intensity distribution (January 1, 2024)

3. NOTO PENINSULA EARTHQUAKE

3.1 Overview of the Noto Peninsula Earthquake

The Noto Peninsula Earthquake occurred at 16:10 on January 1, 2024 (Reiwa 6) with an epicenter 42 km northeast of Anamizu, Hoju, on the Noto Peninsula in Ishikawa Prefecture, Japan. The magnitude of the earthquake was 7.6 with an epicenter at a depth of 16 km. **Figure 7.** shows the location of the epicenter and the seismic intensity distribution [4] and additionally, the figure also shows the damaged areas shown in this paper. The highest seismic intensity observed was 7 on the seismic intensity observed in Monzen Town, Wajima City, Ishikawa Prefecture and Shiga Town, Hakui District. Since the epicenter is close to the epicenter of the Oku Noto Earthquake (May 5, 2023) shown in Figure 1, the magnitude of the seismic intensity itself is different, but the seismic intensity distribution range in Ishikawa, Toyama, and Niigata prefectures is similar. The earthquake caused enormous damage, including the collapse of houses, landslides, and tsunamis, which killed more than 240 people. **Table 3.** summarizes the damage [7].

The Noto region has been experiencing an active earthquake swarm since around December 2020, and the 2024 earthquake occurred in the middle of it. The Japan Meteorological Agency (JMA) named this earthquake and a series of seismic activities since December 2020 the "Noto Peninsula Earthquake in Reiwa 6".

Tremors with a seismic intensity of 1 or higher were observed in 45 prefectures, including almost all of Honshu and Shikoku and parts of Kyushu and Hokkaido, excluding Nagasaki and Okinawa. This magnitude 7.6 earthquake is the largest earthquake observed in the Noto region of Ishikawa Prefecture since records are kept in 1885 (Meiji 18), and exceeds the magnitude 7.3 of the 1995 Hyogo Prefecture Southern Earthquake (Great Hanshin-Awaji Earthquake) and the 2016 Kumamoto Earthquake. Collapse of buildings, damage from tsunamis, uplift of the ground, and liquefaction have also been confirmed.

Table 3. Damage situation (Noto Peninsula earthqueke)

	Prefecture		Niigata	Toyama	Ishikawa	Fukui	Nagano	Gifu	Aichi	Osaka	Hyougo	Total
Human casualties	Dead person				241							**241**
	Missing person											
	Injured person	Serious wound	5	3	312							**320**
		Minor injury	44	44	872	6		1	1	5	2	**975**
	Total		49	47	1,425	6		1	1	5	2	**1,536**
Damage to houses	Complete destruction		93	129	6,528							**6,750**
	Half destruction		2176	340	5,189	9						**7,714**
	Partially damaged		13619	6,975	13,962	126	12					**34,694**
	Flooding above the floor				6							**6**
	Flooding under the floor		14		5							**19**
	Total		15902	7,444	25,690	135	12					**49,183**

Figure 8. House and building in **Wajima** that collapsed due to the earthquake

Figure 9. Morning Market Street (**Wajima**) where the fire occurred

In this earthquake as well, the most severe damage occurred in areas with high seismic intensity, as shown in **Figure 7**. Not only houses but also buildings collapsed (**Figure 8**. intensity 6-), and fire extinguishing was delayed due to water outages and the risk of a tsunami, and large-scale fires broke out in Wajima and other areas (**Figure 9.** intensity 6-). Immediate recovery is required to allow evacuees to return to the Wajima city area due to direct earthquake damage and fire damage.

3.2 Damage caused by the Noto Peninsula Earthquake

In Sotoura on the Noto Peninsula facing the Sea of Japan, there are many steep mountainous areas approaching the coast. As a result, this earthquake caused slope disasters such as slope collapses in many areas. **Figure. 10.** shows the slope collapse on the east side of the Yase cave gate in the Maura district of Suzu City (intensity 6-). The May 2023 earthquake caused rockfalls and slope collapses, and the road was protected by sandbags installed at the time. However, the earthquake in January 2024 caused a large-scale slope collapse and the road is currently closed. **Figure 11.** shows a slope collapse that occurred on the west side of the Osaka tunnel in Maura area (intensity 6-). It can be seen that the wellhead is completely blocked. In Nie, Suzu, multiple slope failures occurred, and nine precious lives were lost. **Figure 12.** shows the slope collapse of Nie, but many boulders on the slope can be confirmed (intensity 6-). **Figure 13.** shows the reinforcing earth retaining wall capturing the sliding of a cliff cone that occurred in January 2024 in the Suzu Maura area (intensity 6-). However, the A rockfall disaster occurred on this slope in 2006, so a reinforced earth protection retaining wall was constructed to protect against falling rocks. During the slope failure that occurred this time, the retaining wall was able to capture a large amount of the earth and sand, but in some areas the retaining wall was pushed

toward the road side. At the time of the earthquake, uplifts of up to 4 meters occurred on the coast in this area of the Noto Peninsula facing the Sea of Japan. **Figure 14.** shows the collapse of the window rock (intensity 6-), which is a tourist attraction in Sosagi, Wajima, and the uplift of the ground can be also confirmed. **Figure 15.** shows the slope collapse of the Wajima-

Before the Noto Peninsula Earthquake (May 2023)

After the Noto Peninsula Earthquake (January 2024)

Figure 10. Yaseno cave gate seen from Suzu side

Figure 11. Suzu **Maura** (slope collapse at the west side of the Osaka tunnel)

Kumano Tunnel wellhead (intensity 6-), and the destruction of the high-energy protection net has been destroyed, and it is now protected by sandbags. **Figure 16.** shows the accumulation

Figure 12. Slope collapse (Suzu **Nie**)

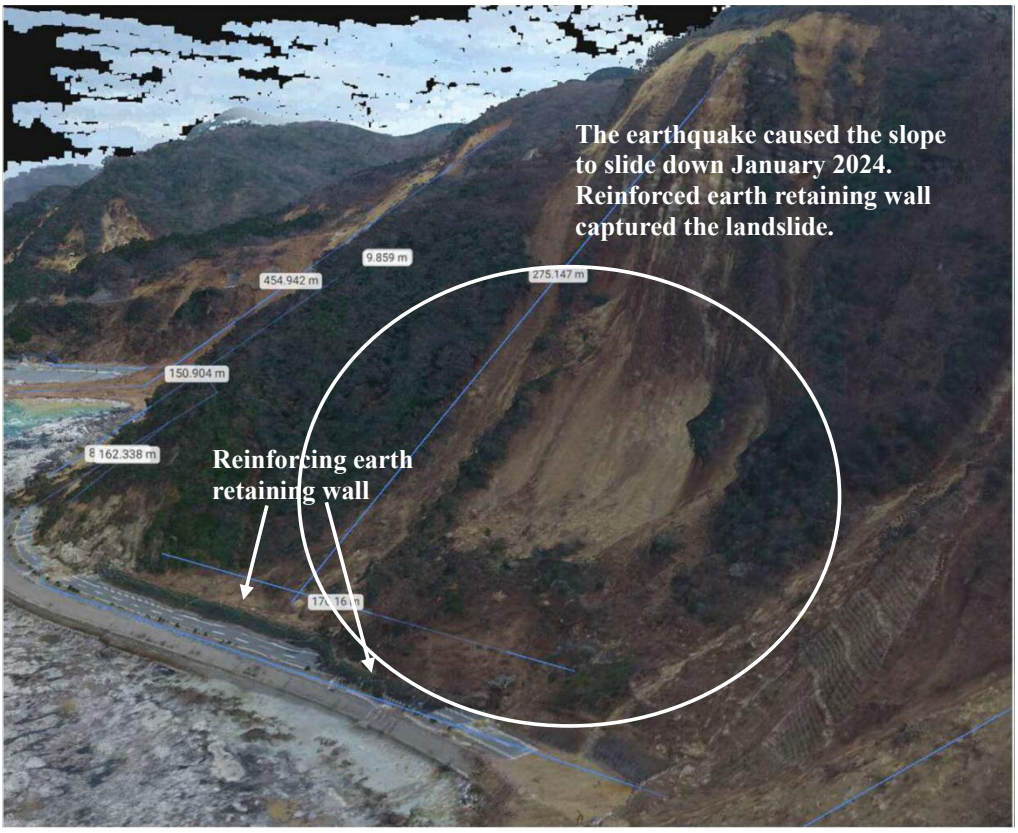

Figure 13. Suzu **Maura** (Sediment capture by reinforced soil retaining wall)

of sediment on the snowshed and the slope collapse at the Hone River in Mitsui, Wajima (intensity 6-).

Here, some damage caused by the earthquake is shown, but in the case of the Noto Peninsula earthquake, as shown in **Table 3.**, it was severely damaged. We would like to express my condolences to those who lost their lives and my heartfelt sympathies to the bereaved families

Figure14. Collapsed window rock (Wajima **Sosogi**)

Figure 15. The wellhead of the Wajima **Kumano** Tunnel

Figure16. Sediment accumulation on snowshed and slopefailure (Wajima **Mii Motoe**)

and those affected by the disaster. There are still many people who have been forced to evacuate, and We sincerely hope that the entire nation will work together to advance the relief and recovery work as soon as possible.

CONCLUSIONS

This paper provides a detailed report on the Noto Earthquake that occurred on May 5, 2023 and the Noto Peninsula Earthquake, which occurred seven months later on January 1, 2024, as well as the extent of the damage, as well as the prospects for the future and requests for cooperation. They are summarized below.

- The largest earthquake in the series of seismic activity up to May 31, 2023 was a magnitude (M) 6.5 earthquake that occurred on the Noto Peninsula at 14:42 on May 5, 2023, with a maximum seismic intensity of over 6 in Ishikawa Prefecture and a long-period seismic motion class 3 in Noto. This earthquake was named the Okunoto earthquake in the 5th year of Reiwa.
- The Okunoto Earthquake in 2023(Reiwa 5) caused 49 human casualties, including one death, and damage to 3,397 houses, including 40 completely destroyed.
- The Okunoto Earthquake in Reiwa 5 caused 49 human casualties, including one death, and damage to 3,397 houses, including 40 completely destroyed. Up to 39 households were cut off, but they were resolved by May 7. National Highway 249 was closed in two places in Suzu City and Wajima City due to falling rocks and widening cracks in the road surface, but by May 10, one-way alternating traffic was possible.
- At 16:06 on January 1, 2024 (Reiwa 6), an earthquake of magnitude 5.5 occurred off the coast of the Noto Peninsula in Ishikawa Prefecture, and a maximum seismic intensity of 5 or more was observed in Suzu City, Ishikawa Prefecture. Immediately afterwards, at 16:10, an earthquake of magnitude 7.6 occurred in the Noto region, and tremors with a seismic intensity of 7 were observed in Wajima City and Shiga Town. This earthquake was named the Noto Peninsula Earthquake in 2024(Reiwa 6).
- The damage caused by the Noto Peninsula Earthquake in Reiwa 6 was extremely severe, with 1,538 human casualties, including 241 deaths, and damage to 76,257 houses, including 9,050 completely destroyed. There were also 17 fires.
- The situation of several slope disasters such as rockfalls caused by earthquakeswere concretely reported.

ACKNOWLEDGMENTS

We would like to express my condolences to those who lost their lives and my heartfelt sympathies to the bereaved families and those affected by the disaster. There are still many people who have been forced to evacuate, and We sincerely hope that the entire nation will work together to advance the relief and recovery work as soon as possible. We would also like to express my deepest gratitude to everyone who cooperated in the research for this paper.

REFERENCES

[1] The Coordinating Committee for Earthquake Prediction, Japan: Results of the study on crustal activity monitoring, 235th regular meeting, 2022.

[2] Headquarters for Earthquake Research Promotion Earthquake Research Committee: Evaluation of seismic activity in the Noto region of Ishikawa Prefecture, Headquarters for Earthquake Research Promotion Earthquake Research Committee, 2023.

[3] Japan Meteorological Agency Earthquake and Volcanology Department (2023). Earthquake in the Noto region of Ishikawa Prefecture around 14:42 on May 5, Reiwa 5.

[4] Ishikawa Prefectural Crisis Management Supervisor's Office Crisis Countermeasures Division (2023). Application of the Disaster Relief Law for the earthquake with the epicenter in the Noto region of Ishikawa Prefecture in the 5th year of Reiwa.

[5] Cabinet Office Emergency Disaster Response Headquarters (2023). Regarding the damage status related to the earthquake with the epicenter in the Noto region of Ishikawa Prefecture, Reiwa 5/5/18 8 At 0 0 minutes current.

[6] Cabinet Office Emergency Disaster Response Headquarters (2023) Regarding the damage status related to the Noto Peninsula Earthquake in Reiwa 6, Reiwa 6/1/2 7:0 0 minutes current.

[7] Cabinet Office Emergency Disaster Response Headquarters (2023) Regarding the damage status related to the Noto Peninsula Earthquake in Reiwa 6, Reiwa 6, February 22, 1 4:00 as of 1 4:00.

VEHICLE SECURITY BARRIER AS A COUNTER-MEASURE FACILITY AGAINST DELIBERATE AND ACCIDENTAL VEHICLE IMPACT

Tat-Seng Lok[1], Chin-Teck Ong[2], Alistair Crooks[3]

[1] Er. Dr, Protective Security Advisor & Former Academic (Ret'd), PHM Technologies Pte Ltd, Singapore 367956
dr.tslok@gmail.com

[2] Mr, Director, B P (Systems) Engineering Pte Ltd, 20 Shaw Road, Ching Shine Industrial Bldg, #04-09, Singapore 367956
danny@bpsystems.com.sg

[3] Mr, Solutions Leader, Horiba Mira Ltd, Watling Street, Nuneaton, Warwickshire, CV10 0TU, United Kingdom
Alistair.crooks@horiba-mira.com

Corresponding Author: Tat-Seng Lok BSc(Hons), PhD, CEng, FIStructE, Principal Member of RSES(UK), EurIng, MIExpE(UK), Specialist PE(Protective Security-S'pore), PE(Civil-S'pore), Competent Person (IPA/CPS-S'pore)
PHM Technologies Pte Ltd, 20 Shaw Road, #04-09, Singapore 367956
Email: dr.tslok@gmail.com

ABSTRACT

The authors had provided the background to, and highlighted the importance of, testing vehicle security barriers (VSB) to prevailing Test Standards. This paper provides an update of surface-mounted VSBs in view of the recently-approved International Organization for Standardization document that has superseded previous Standards where they have been specified in many security projects around the world. The current US Standard remains applicable as a compliant document although this is mainly used outside of Europe. The differences between the ISO document and a previous withdrawn Standard are stark. The classification of test results in ISO now includes, *inter alia*, debris of a lower mass, different penetration measurement points, and an increased number of vehicle types to reflect a global vehicle fleet. This paper addresses many of the issues that may require risk assessors and security engineers to rethink new threats going forward. A comparison of the major differences between the various test Standards used in risk assessment methodology are provided. Results from a recently-tested surface-mounted reinforced concrete VSB with an integrated security fencing is discussed. The VSB was conceptualised from a preliminary momentum-based design approach to derive a preliminary barrier, and then modified accordingly to fit the specification.

Keywords: *Vehicle Security Barrier, Test Standards, Full-Scale Testing of VSB with Integrated Security Fencing, Compliance.*

1 INTRODUCTION

Security barriers are specified and used extensively to safeguard space, infrastructures and the public against accidental or deliberate penetration by vehicles. They are basically developed to separate social space/people/infrastructure from vehicles.

The majority of motor vehicles are used by people with good reasons on use. This includes self-driven and electric vehicles. However, all vehicles may be deliberately acquired for criminal purposes, by hijacking hire or theft, and used as a weapon of destruction. Hostile actors that acquire vehicles for violent use have intentions to cause significant hazards to the public and disruption of infrastructure, thus attracting worldwide media focus. For these reasons, areas with high pedestrian flows, iconic buildings, critical infrastructures, etc., are protected in one form or another by security barriers. The successful use of bollards/planters at bus stops, or at approach entrances with gradient to underground car parks that are commonly seen in many countries with surface space constraints.

To protect the public and infrastructure, vehicle security barriers (VSBs) were developed to resist impact forces from existing vehicles, and the corresponding barriers were designed accordingly. The types of vehicles were limited in the past when VSBs were considered. Today, many Standards recognise the range of family saloons, commercial vehicles and the large stock of heavy goods vehicles that are designed for daily use. As the number of vehicles and vehicle categories increase, so too are the potential threats and vulnerability of existing barriers. Clearly, the number of vehicles are expected to rise significantly due to interests in electric vehicles.

To ensure vehicles are separated from the public, property or infrastructure, many features of traffic engineering can be employed, such as raised kerbs, trees and hedges lining the stretch of road. More drastic measures include drains, ditch and wall. As cities and the business environment evolved, secured barriers were developed to meet the evolution of changing landscapes and vehicle types. The authors highlighted the importance of testing[1] a vehicle security barrier to the prevailing Test Standard, to match infrastructure protection, public space and safety requirements. Any mis-match of potential threat/vulnerability in risk assessment could result in costly consequences.

In this paper, an update on VSB testing methodology is presented and focuses on the most recent document[2] that has been accepted by some jurisdictions. This document has superseded Ref.[3] at the time of writing this paper. It is probable that in a new setting, the withdrawn document[3] may not be applicable to reduce the risks. The authors shall not dwell on Refs[4,5] since these two documents were widely discussed[1], and are currently under review at the present time.

For other forms of attack, security engineers may access other documents[6,7] to consider intruder resistance. This paper addresses only the testing of vehicle security barriers and focuses on major differences and comparisons between all currently-used documents in risk assessment

methodology. The authors suggest that risk assessors consider reviewing current threat/vulnerability to ensure compliance in the light of new test criteria for VSBs.

The paper ends with a brief description of an approach using momentum as the basis for a preliminary design of a reinforced concrete VSB. The initial design was then modified to fit specification and to fabricate a full-scale test duplicate specimen with an integrated security fence at the test site. The crash test was successfully conducted in 2023 prior to the implementation of the current Standard[2], but had nevertheless satisfied the requirements of this draft document.

2 PRESENT/IN-USE STANDARDS[3-6]

These standards had been discussed, including highlighting a typical VSB test of a surface-mounted RC wall complete with an integrated anti-climb fencing and razor-sharp security barrier. In view of increasing risks of delay attack strategy, a mention is made here of the vehicle attack delay standard [6]. Vehicle attack delay standard is a concept used to test VSBs that provide a lower level of protection than those tested to previous Standards described previously[1].

The aim of VADS is to use the attacking vehicle to breach the test barriers/items, without immobilising the vehicle or driver, and thus gaining vehicle or pedestrian access to a protected space to further accentuated vehicle as a weapon attack. As the title implies, VADS is a delay rating system based that the VSB is able to sustain the attack from the specified vehicle/threat.

Types of perimeter and temporary barriers are available[2] to cope with VADS threats. These VSBs are often used for temporary protection and are not fixed to the ground. Many such systems exist such as wheel entanglement systems, concrete blocks, water-filled inter-connected barriers and strategically-positioned static vehicles. Semi-permanent barriers such as flower stands, street furniture can equally be assessed to mitigate vehicle as weapon (VAW) threats within a community/event setting.

In jurisdictions where the probability of multiple attacks is clearly advised in large public gatherings in open space, it is essential that VADS is taken seriously and security assessors are armed with the appropriate counter-measures. Manual attack [2,7] is consistently implied in test Standards with explicit qualifications stating that it does not cover assessment of the test item against attack from multiple vehicles either in concurrent or follow-on attack. Note that threat scenarios are applied differently to permanent VSBs.

3 CURRENT STANDARD[2]

The principles of this Standard is no different to previously available documents in the broader scope of protecting people, private space and infrastructure from the threat of potentially hostile or accident-related incidents. A vehicle-borne threat could arise from a vehicle theft or from a terror-related incident scenario designed to maximise harm and damage. For accident-related cases, the possibility of brake/mechanical failure or from a medical condition rendering the

innocent driver immobile but in-charge of a vehicle, approaching a steep gradient leading to an underground carpark. Thus, this Standard is applicable to risk assessors of general "vehicle-borne threats", including those responsible for VSB manufacturing, construction specialists and VSB test houses.

There is a tendency of specifiers of VSBs to overlook the situation and view the new Standard as another barrier to construction progress. Nonetheless, the new standard[2] is currently in force, with some jurisdictions accepting previously-tested VSBs as complying with prevailing security threats. Those VSBs tested before the acceptance deadline would be accepted but may be subject to other provisions to ensure strict compliance with safety measures, professional risks and insurance liability.

The basis of the testing and rating depends solely on vehicle type, vehicle mass, and speed of the vehicle. Thus, the document specifies the impact performance requirements for VSBs and a test method for rating its performance. The performance rating is the underlying criterion to prevent limited penetration of a vehicle into usable space. The life of the vehicle classed N1 and above is specified as less than 15 years. Many jurisdictions also require the vehicle to be certified "fit for use" at the time of testing and is issued with an approved Ministry of Transport (MOT) Certificate. For test houses, it is conditional that the site has a 25-metre perimeter from the point of impact.

Occasionally, risk assessors have genuine concern on soil condition of surface-mounted barriers, road surface characteristics or topography of the surrounding. In extreme cases, weather conditions may also be considered. These concerns are easily addressed by engineers at certified test houses and where soil testing and surface preparations can be arranged. Guidance on the selection and specification of a VSB by type and operational suitability is available[8]. This second part provides recent updated guidance on selection, installation, and use of surface-mounted VSBs. The document describes the process of reproducing operational requirements of VSBs and gives clear guidance on a design method for assessing its performance. By implication, this document is applicable to end users such as owners and consultants who specify VSBs that are specifically designed for use to protect people in a public or private space against potential vehicle-borne attacks.

Both parts[2,8] do not apply to the performance of test VSB when subjected to additional interference caused by slow speed nudging and ramming, blast explosion, ballistic attack, manual attack (e.g. with other vehicles or tools or electronic interference/manipulation on the control systems). For prevention of secondary manual intruder resistance, specifiers should refer to appropriate intruder/force entry resistance Standards.

The current Standard defines critical points or measurements, including definitions of VSBs, which are necessary since vehicle impact is defined as the "sequence of events between a moving vehicle engaging with a vehicle security barrier". Categories of vehicles, VSB and how

penetration is measured and vehicle position after impact are shown. In US practise[9], risk assessors may refer to "anti-ram devices" for more details.

3.1 Types of vehicles and vehicle datum point

The vehicle type and VSB is defined and represented pictorially, especially for the commonly-used N1, N2 and N3 vehicle types as shown in Figure 1. The vehicle datum point is shown as a point and defines the position of the post-penetration vehicle, either facing the direction of impact or in a reverse position.

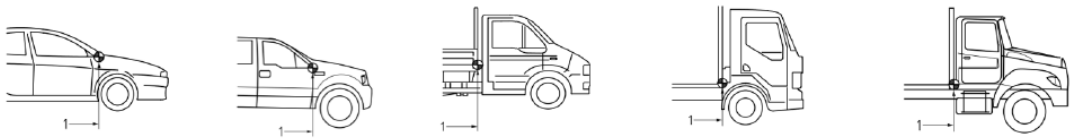

(a) Car (N1) (b) 4x4 crew cab pick-up (N1G) (c) Day cab vehicle (N1) (d) LGV (N2A, N3C, N3D, N3F & N3G) (e) LGW (N2B & N3E)

Figure 1. Vehicle type and vehicle datum point (shown as a target on each type of vehicle)

3.2 Vehicle security barrier – descriptions

Many generic forms of VSBs are possible, where each may be used in a variety of applications. Figure 2 shows a few examples of surface-mounted VSBs and the definition of each of the parts associated it. Every part is numbered and defined accordingly and is consistently used throughout. A number of VADS VSBs are also included.

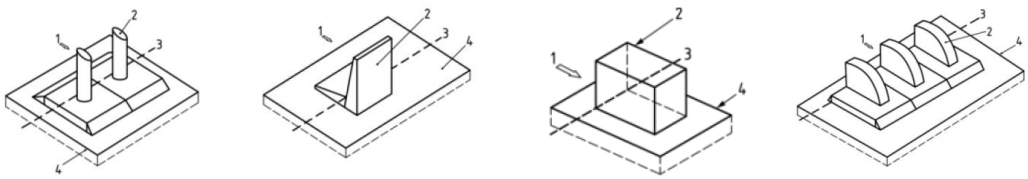

1 = Direction of impact; 2 = VSB; 3 = VSB datum line; 4= Ground level
(Note that the VSB datum line is at the front/impact face of the VSB)

Figure 2. Surface-placed vehicle security barriers and definition of parts

3.3 Major debris

Major debris is defined as any piece of VSB, vehicle or ballast dislodged/detached during the vehicle impact whose mass is ≥2 kg. The mass is reduced from 25 kg in previous Standards[3.4]. The maximum major debris dispersion is measured to the furthest edge of the largest outermost piece of debris. Test "failure" is noted when a mass ≥2 kg is located outside the 25-metre range of the VSB.

3.4 Additional vehicles to reflect a global fleet

New vehicles categories have been added to reflect current vehicle fleet. Additional test vehicles are shown in Figure 3 with corresponding vehicle classifications and mass:

Vehicle Classification	Test Mass	Gross Vehicle Mass	Image Credit ISO 22343-1
N2B 2-axle rigid cab behind (axle)	Was 7,200 kg Now 6,800 kg	Was 12,000 kg Now 14,970 kg	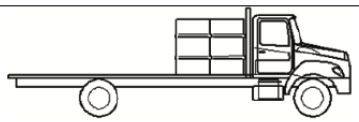
N3D 2-axle rigid cab over	12,000 kg	Was 15,000 kg Now 20,500 kg	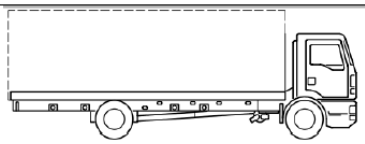
N3E 3-axle rigid cab behind tipper	Was 24,000 kg Now 29,500 kg	27,300 kg	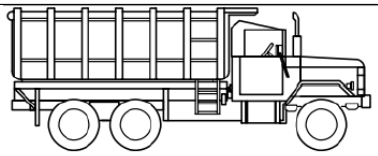
NEW N3F 3-axle rigid cab over	24,000 kg	26,000 kg	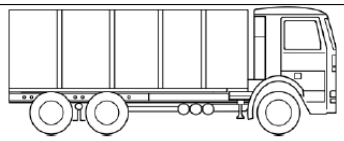
N3G 4-axle rigid cab over (previously N3F)	30,000 kg	Was 32,000 kg Now 36,000 kg	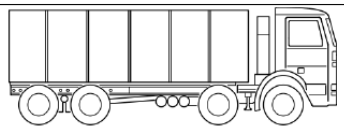

Figure 3. Types of additional vehicles to reflect global changes

3.5 Demand on Test House

Test houses must provide cameras capable of recording the impact sequence from at least 5 metres pre-impact to 25 metres post impact. The test site must be levelled and provide a minimum distance beyond the tested VSB to meet the maximum penetration distance. VSB test preparations and pre/post impact data are more demanding than in previous procedures.

Test report must now summarise, *inter alia*, the form and structure of the VSB, foundation, road surface, impact energy of test vehicle, measurements and position of the furthest debris, and possibly the vehicle deceleration following the impact. Such extent of reporting ensures consistency and safety of the tested product.

Finally, a performance rating classification code is presented by the Test House. This format is similar to previous Standards[3,4] and with the inclusion of major debris ≥2 kg. An example performance rating may be shown as:

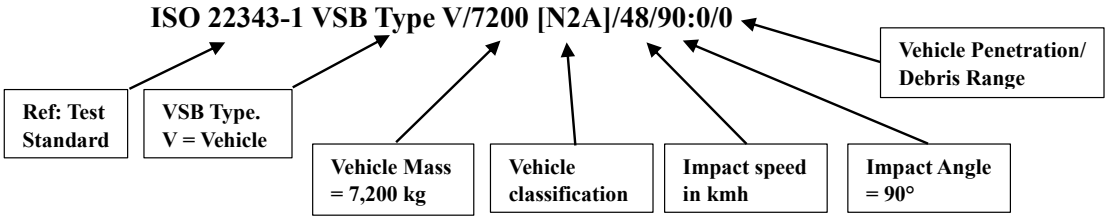

4 SUMMARY OF ISO 22343-1

From the authors' experience in managing testing of VSBs, a summary list may be presented:

(1) Terminology – more specific in describing the VSB, for example as "*Surface placed VSB*" instead of "*Free standing VSB*".
(2) Debris ≥2 kg mass of the VSB, vehicle or fencing are classified and recorded. The furthest debris ≥ 2 kg mass strewn on the test site is recorded.
(3) Vehicle penetration and debris is measured from the front (impact face) of the VSB.
(4) Penetration (measured from datum of the VSB to the datum of the test vehicle) greater than 25 metres is "failure" and is not rated. Penetration acceptance is defined by user.
(5) VSB manufacturer must submit full details of the product and documentation to the Test House before the test.
(6) The new Standard has added various vehicle categories not considered in other Standards. However, a number of vehicles have been identified as "equivalent" to US Standard.
(7) Test vehicle age limit is restricted to less than 15 years for vehicles classed as N1 and above (see Figures 1 and 3). Vehicles must be certified "fit for use" at the time of testing.
(8) It is incumbent of Test Houses to check and report that test vehicle dimensions and tolerances are within prescribed limits (e.g. total mass is ±5kg and ±25kg for smaller and larger vehicles respectively).
(9) Strength of concrete derived from cube/cylindrical tests of the VSB is the minimum strength specified for on-site project installation.
(10) Performance rating classification is similar to the previous format but includes major debris range.

It is the responsibility of VSB manufacturers and specialist contractors to ensure that their on-site test observations, including site conditions, are in order before the test vehicle is launched. The ISO document acknowledges alternative modes of attack and resistance to force entry, which are covered in other test methodologies. It explicitly excludes modes of attack such as slow speed encroachment, nudging, ramming, manual attacks manipulation of the VSB and control systems by any means (e.g. physical, electronic).

In conjunction with the above listed ISO highlights, a comparison of major differences with previous Standards may be tabulated as shown in Table 1.

ISO 22343-1[2] (Current)	**PAS 68**[3] (withdrawn)	**IWA-1**[4] (ISO version withdrawn)	**ASTM F2656/ F2656M:23**[5] (Current)
Ten vehicle type categories	**Six** vehicle type categories	**Nine** vehicle type categories	**Six** vehicle type categories
Impact speed 16-112 km/h. Optional: oblique attack.	Impact speed 16-112 km/h. Optional: oblique attack.	Impact speed 16-112 km/h. Optional: oblique attack.	Impact speed 48-100 km/h. 90° impact angle only.
Penetration measured from **front face of VSB**. Value is quoted in rating.	Penetration measured from **rear face of VSB**. Value is quoted in rating.	Penetration measured from **front face of VSB**. Value is quoted in rating.	Penetration measured from **front face of VSB**. P1 rating is provided if penetration is less than 1.0m, after which value is quoted in rating.
Major debris is ≥ 2 kg. Debris position measured from front (impact) face of VSB and quoted in rating.	Major debris is ≥ 25 kg. Debris position is measured from **rear face of VSB** and quoted in rating.	Major debris is ≥ 25 kg. Debris position is measured from **front face of VSB** and quoted in rating.	Debris mass is not used. Debris position is measured from front face of VSB and quoted but not part of rating.
Test vehicle N1 and categories (see Figures 2&4) is less than **15 years old**.	Test vehicle N1 and categories above is less than **10 years old**.	Test vehicle N1 and categories above is less than **10 years old**.	Test vehicle M and categories above[5] is less than **10 years old**.
Max speed of 7.5 Tonne vehicle (N2A) is 80 km/h.	Max speed of 7.5 Tonne vehicle (N2) is 64 km/h.	Max speed of 7.5 Tonne vehicle (N2A) is 80 km/h.	Max speed of M/C7 vehicle is 80 km/h.
Rating description: **V/7200(N2A)/64/90:2.4/10.2**	Rating description: **V/7500(N2)/64/90:2.4/10.2**	Rating description: **V/7200(N2A)/64/90:2.4**	Rating description: **M40-2.4**

Table 1. Main differences of various Test Standards

5 SIMPLIFIED DESIGN OF VSB

Engineers may wish to consider the principles of momentum to initiate design of a security wall to resist the kinetic energy imparted from a speeding vehicle. Security engineers, however, shall consider, *inter alia*, the vulnerability of the protected space, likely attack angle, vehicle type, approach speed, surface texture, gradient, etc.

During the impact process, the vehicle crumples, vehicle parts are dislodged, the VSB wall itself may be breached/eroded with dispersion of concrete/steel elements, and parts of the security fencing (if installed) may be ejected. The ISO document demands that account is taken of debris ≥2 kg mass resulting from the VSB. Indeed, VSB deformation (uplift and lateral displacement) may occur in tests. Thus, energy losses are inevitable. Nevertheless, a conservative estimate of the impact force may be obtained in a preliminary design of the vehicle security barrier against vehicle impact.

From first principles of linear momentum, the rate of change of momentum, M, may be expressed (assuming no energy loss) as:

$$M = (P_f - P_i)/t \tag{1}$$

where "P_f" and "P_i" are the final and initial momentum of the moving vehicle and "t" is the duration of impact (vehicle in contact with VSB). Strictly, "t" should be written at "$(t_f - t_i)$", where "t_f" and "t_i" are the final and initial contact time of the vehicle respectively. However,

the initial time is usually taken as zero at the point of impact in the same way as the arrival of a blast pressure wave from a distance imparting a fixed target.

Equation (1) may be re-written as:

$$M = (m_f.v_f - mi.vi)/t \quad (2)$$

Where "m_f" and "m_i" are the final and initial mass of the vehicle respectively, and "v_f" and "v_i" are the corresponding final and initial linear velocity of the vehicle.

Assuming zero loss of vehicle mass upon impact:

$$M = m.(v_f - vi)/t \quad (3)$$

But, acceleration, A, is defined as:

$$A = (v_f - vi)/t$$

Thus, the rate of change of momentum, M, is:

$$M = m.A \quad (4)$$

Assuming zero loss of mass of the vehicle upon impact, which from the Author's experience is strictly not true, the rate of change of momentum is the vehicle impact force.

Further, there are other factors influencing the impact such as ground friction, ballast distribution, vehicle veering upon impact and crumple zones of frontal vehicle components prior to impact contact of the vehicle engine/chassis and VSB. More importantly, the duration of vehicle impact is not an instantaneous rise, nor a sudden decay, of the impact force, as often defined in rectangular impulse load cases. Observed acceleration-time histories often show a gradual increase and decay as typical characteristics of vehicle impact. Thus, the calculated impact force is clearly conservative, and provides an excellent preliminary estimate of the force required to design the reinforced concrete target.

Test specialist should also be aware that when a security fence is installed as part of the test (representing actual on-site project installation), then the same fencing should be installed in exactly the manner and using the same components on the test target. Note that all debris ≥2 kg includes the fencing parts (steel mullions, transom, fencing, razor coils, nuts/bolts). Any part or attached parts ≥2 kg must be identified, located in the test space with respect to the target within the 25m perimeter of the test site. This requirement is essential when a VSB is constructed close to a facility where vehicle penetration and/or debris pose significant hazards to building, equipment and personnel inside the compound.

6 TESTING & IMPLEMENTATION

A test on a surface-mounted reinforced concrete VSB together with security fencing using the above approach was designed. During the construction phase, concrete cubes were obtained and known strength of primary/secondary bar reinforcements were noted. On completion of the target wall, mullions/transoms were erected and secured before the security fencing was positioned as specified in the project. Finally, a topping of razor-sharp fence was installed.

Following the vehicle impact test, the fencing was observed[1] to be intact at the point of impact with the remaining unaffected fence secured. The area surrounding the target was surveyed for debris ≥2 kg of dislodged parts from the:

- vehicle,
- wall, and
- fencing.

To characterise the rating, the distance from the front of the VSB to the vehicle datum (affixed target marker prior to the test) was measured. Despite the penetration of the cab, the rated penetration was zero because the vehicle datum point did not exceed the VSB datum point in the direction of travel. Thus, this reinforced concrete barrier with security fencing satisfied all the requirements of the new ISO document[2]. Under the previous classification, the wall also complied with all the requirements of previous Standards[3,4].

This surface-mounted tested VSB has been successfully installed. The designed VSB can be used where the road surface level is horizontal or at a gradient (using stepped foundation) as shown in Figure 4.

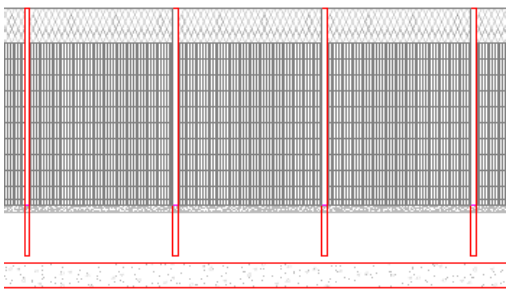

Elevation

Figure 4a. Horizontal surface-mounted VSB

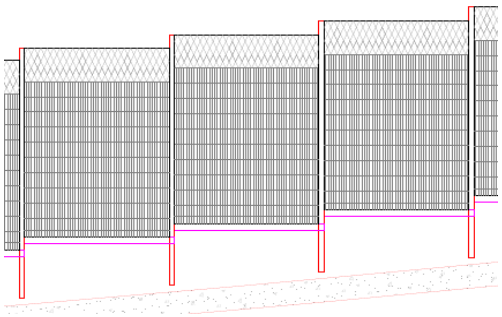

Elevation

Figure 4b. Stepped foundation surface-mounted VSB

Figure 4. Constructed surface-mounted VSB with security fencing

Based on the simplified approach above, an initial reinforced concrete block was derived to provide the basis to optimise the design to fit the specification of the site. The proposed approach has shown the benefits of using simplified engineering principles to design and to test several reinforced concrete VSBs over a period of 3 years.

Computational analyses using specialised vehicle models and complex modelling techniques to include vehicle soft and hard parts are available. Indeed, concrete and vehicle erosion may be accounted for in the analyses. Such software and analyses techniques are excellent tools for engineers to visualise the sequence of impact, in studying barrier/vehicle interaction and design. However, the prohibitive licensing costs and essential specialised training make such software inaccessible for use by the majority of small to medium-sized engineering consultancies and specialists, whose main livelihood continues to depend on conventional civil and structural engineering projects.

7 CONCLUSIONS

The main parts of a new ISO Standard were discussed and compared with previous Standards, which are currently in use by engineers specifying the requirements of vehicle security barriers. Some security jurisdictions have implemented acceptance of VSBs tested to the new Standard due to current security risk analysis. VSBs tested to previous Standards may continue to be accepted but they may not satisfy the additional requirements in a new setting that security specialists identify as hazards in their present risk assessment. Simplified but conservative principles of momentum were shown to enable engineers to design VSBs. However well the VSB is designed, there is no better approach to physical testing. An example showed a surface-mounted reinforced concrete VSB had complied with the new requirements, as well as all the previous Standards [3,4] mentioned in this paper.

8 ACKNOWLEDGEMENTS

We gratefully acknowledge the many experts, especially the staff from Highway Safety & Protection of Infrastructure, MIRA, UK, who have far greater experience in VSB testing/Standards, for their advice and council over many years of engagement. We acknowledge using diagrams and some text available in publicly-available documents since there are no better descriptions or pictorial representations to describe them to clarify our point. To all the other people who have provided valuable feedback, we thanked them for their generous sharing of views that had added to our education on HVM/VAW methodology.

9 DISCLAIMER

Views and opinions of the Authors are based on available publications in the public domain and experience of the Authors in analysing, designing and testing of VSBs. Full-scale test failures are expensive in any form. However, it is from failures that we learned to tackle the intricacies of supervision, material characteristics, concise communication, logistics and construction. Nevertheless, this paper should not be considered as expert advice since the probability of failure of a single test could arise even if the VSB had been adequately designed with a high factor of safety. Thus, we accept no responsibility of engineers using our approach to design VSBs for testing.

10 REFERENCES

[1] A Crooks, TS Lok and CT Ong, Vehicle security barriers – specification and compliance testing, *Proceedings of 14th Int Conf on Shock and Impact Loads on Structures*, pp17-26, Singapore, ISBN: 978-981-18-6586-2, Ed TS Lok & CK Ang, Mar 2023.

[2] ISO 22343-1:2023, Security and resilience. Vehicle security barriers Part 1: Performance requirement, vehicle impact test method and performance rating, *International Organization for Standardization*, Switzerland, 30 Sept 2023. (corresponding British Standard BS ISO 22343-1:2023, 31 Jan 2024).

[3] PAS68:2013, Impact test specifications for vehicle security barrier systems, *Publicly Available Specifications, British Standards Institution*, 2013.

[4] IWA14-1:2013 – Vehicle Security Barrier: Part 1: Performance requirement, vehicle impact test method and performance rating, *International Worksop Agreement*, 2013.

[5] ASTM F2656-7: 2015, Standard test method for vehicle crash testing of perimeter barriers, *American Society for Testing and Materials*, 2015.

[6] NPSA, Introduction to vehicle attack delay standard (VADS), *NPSA*, UK (Official), 2019.

[7] LPS 1175; Issue 8.0, Requirements and testing procedures for the LPCB certification and listing of intruder resistant building components, strongpoints, security enclosures and free-standing barriers, *BRE Global*, UK.

[8] ISO 22343-2:2023, Security and resilience. Vehicle security barriers Part 2: Application, *International Organization for Standardization*, Switzerland, Sept 2023. (corresponding British Standard BS ISO 22343-2:2023, 31 Jan 2024).

[9] FEMA 426, Reference Manual to Mitigate Potential Terrorist Attacks against Buildings, *Federal Emergency Management Agency, US Dept of Homeland Security*, Dec 2003.

PROTECT2024